

# **An Experimental Study of Radial Electric Field and Bootstrap Flow on the HSX Stellarator**

by

Tom J. Dobbins

A dissertation submitted in partial fulfillment of  
the requirements for the degree of

Doctor of Philosophy  
(Nuclear Engineering Engineering Physics)

at the  
University of Wisconsin–Madison

2018

© Copyright by Tom J. Dobbins 2018

All Rights Reserved

## Abstract

The neoclassical code PENTA estimates a large positive radial electric field ( $\sim 40\text{-}50$  kV/m) near the core of the HSX plasma. Impurity ion flow measurements have not measured this large electric field, nor do the measured flows match those predicted by these codes. This discrepancy will be examined in this work mainly by improving the diagnostics measurement capability on HSX. Firstly, a synthetic diagnostic has been developed to account for the finite width of the neutral beam and spot size. This is important due to the relatively large beam width compared to the flux surfaces near the core of HSX plasmas. Secondly, the Charge Exchange Recombination Spectroscopy (CHERS) diagnostic on HSX has been modified to measure counter-streaming Pfirsch-Schlüter flows. This diagnostic will be used to find the bootstrap flow and the radial electric field and their evolution throughout the discharge.

For my wife, Maria Rose Dobbins

## **Acknowledgments**

I would like to thank Prof. David Anderson, Dr. Santhosh Kumar, Dr. Simon Anderson, Dr. Joseph Talmadge, Dr. Konstantin Likin, Dr. Chuanbao Deng, and the HSX group for their support throughout my time working on this project. I would also like to thank my parents and all of the love and support they have given me over the years that have brought me to this point. Lastly, I would like to thank my wife, who's love and support helped me through my time as a graduate student.

# TABLE OF CONTENTS

	Page
<b>LIST OF FIGURES</b> . . . . .	vi
<b>1 Introduction</b> . . . . .	1
1.1 The Helically Symmetric eXperiment . . . . .	2
1.2 The Importance of $E_r$ on Stellarators . . . . .	3
1.3 Outline of Thesis Work . . . . .	5
<b>2 Fundamentals of flows and <math>E_r</math> on HSX</b> . . . . .	8
2.1 Neoclassical flows and $E_r$ in Stellarators . . . . .	9
2.1.1 The Helical Resonance . . . . .	15
2.1.2 Electron Root Plasmas . . . . .	19
2.2 Analytic Neoclassical theory for Flows in Stellarators . . . . .	21
2.3 Non-Neoclassical flows and $E_r$ in optimized Stellarators . . . . .	22
2.3.1 ECRH driven torque . . . . .	22
2.3.2 Neutral dampening . . . . .	24
2.3.3 Turbulence driven radial electric field and flows . . . . .	26
2.4 Previous Radial Electric Field and flow Measurements on HSX . . . . .	29
2.5 $E_r$ and Flow Evolution . . . . .	32
2.5.1 Flow and Current Evolution . . . . .	33
2.5.2 PENTA and flow and current Evolution . . . . .	35
<b>3 Pfirsch-Schlüter CHERS Diagnostic</b> . . . . .	42
3.1 CHERS Diagnostic Background . . . . .	42
3.1.1 Fitting and Calibration . . . . .	44
3.2 Pfirsch-Schlüter CHERS Diagnostic Background . . . . .	45
3.3 The Neutral Beam Synthetic Diagnostic . . . . .	51
3.3.1 PENTA Neoclassical Modeling . . . . .	51
3.3.2 The Diagnostic Neutral Beam . . . . .	53
3.3.3 Neutral Beam Model . . . . .	53

	Page
3.3.4 Atomic Physics . . . . .	56
3.3.5 Pfirsch-Schlüter Flow Synthetic Diagnostic . . . . .	60
3.4 Conclusion . . . . .	62
<b>4 Measurements . . . . .</b>	<b>65</b>
4.1 $E_r$ and Flow Evolution measurements . . . . .	65
4.1.1 configuration comparisons . . . . .	67
4.1.2 configuration comparisons . . . . .	67
4.1.3 Heating power and location scan . . . . .	68
4.2 Pfirsch-Schlüter Flow Measurements . . . . .	68
4.2.1 configuration scan . . . . .	69
4.2.2 Heating power and location scan . . . . .	69
4.2.3 Flow vs $E_r$ comparisons with PENTA . . . . .	69
4.3 Conclusion . . . . .	69
<b>5 Conclusion and Future Work . . . . .</b>	<b>78</b>
5.1 Flow Drive . . . . .	78
5.1.1 Ionization region and flow . . . . .	78
5.2 Conclusion and future work . . . . .	79

## LIST OF FIGURES

Figure	Page
1.1 HSX Stellarator . . . . .	2
1.2 HSX plasma Parameters . . . . .	3
1.3 Transport changes with $E_r$ . . . . .	4
2.1 Flow drive and damping sources and sinks . . . . .	8
2.2 Radial Particle Fluxes from PENTA . . . . .	11
2.3 Hamada Spectrum of HSX . . . . .	12
2.4 Magnetic field contours and flow direction . . . . .	13
2.5 Flow direction . . . . .	15
2.6 Ratio of 4,1 mode to next largest mode . . . . .	16
2.7 Tokamak Resonance . . . . .	17
2.8 Flows vs $E_r$ . . . . .	21
2.9 ECRH flux . . . . .	23
2.10 ECRH Torque . . . . .	24
2.11 Neutral Dampening rates . . . . .	25
2.12 Neutral Dampening . . . . .	26
2.13 Turbulence and neoclassical scaling . . . . .	28
2.14 Previous $E_r$ & flow measurements . . . . .	30
2.15 Current profile evolution reconstruction on HSX . . . . .	34



Figure	Page
3.1 Fit of Carbon line . . . . .	45
3.2 Calibration by channel . . . . .	46
3.3 Resolution of the CHERS views . . . . .	47
3.4 CHERS Geometric Factors . . . . .	50
3.5 CHERS Geometric Factors . . . . .	51
3.6 Poloidal cross section of the HSX magnetic flux surfaces and the beam . . . . .	55
3.7 Histogram of $H_\alpha$ signal vs $r/a$ for different optical spot sizes and views . . . . .	56
3.8 Plasma density from ADAS . . . . .	59
3.9 Carbon density from ADAS . . . . .	59
3.10 Synthetic diagnostic of the Pfirsch-Schlüter views . . . . .	61
3.11 Pfirsch-Schlüter flow and $E_r$ measurements . . . . .	61
4.1 density scan . . . . .	70
4.2 50 kW QHS active . . . . .	71
4.3 50 kW QHS and OM . . . . .	72
4.4 100 kW F14 QHS . . . . .	73
4.5 Pfirsch-Schlüter flow and $E_r$ measurements . . . . .	74
4.6 Flow vs $E_r$ comparisons in QHS . . . . .	75
4.7 Flow vs $E_r$ comparisons in F14 . . . . .	76
4.8 F . . . . .	77
5.1 100 kW QHS CW vs CCW . . . . .	80

## Chapter 1

### Introduction

Nuclear fusion is a potential solution to the Earth's long term energy problems. It is clean source of energy, it has a very large supply of fuel, and does not produce high level radioactive waste like its counterpart, fission. Fusion works by combining light nuclei, typically the hydrogen isotopes Tritium and Deuterium, to create a neutron and a helium atom and releases a large amount of energy. Although fusion has many advantages over other power sources, it has proved difficult to create a reactor that can create more fusion power than is required to start the fusion reaction. There are several pathways currently being investigated to solve this problem, and the leaders are tokamaks, stellarators, and laser driven implosion devices. Tokamaks and stellarators work in a similar way, by confining high temperature plasmas in carefully designed magnetic fields. Tokamaks are the leading fusion concept due to their good confinement and the relative simplicity of their design. Tokamaks have many issues, that if unsolved, could make them unworkable as a reactor. The main problems include disruptions and maintaining the plasma in steady state conditions. Stellarators are inherently steady state and avoid the current driven disruption problem found in tokamaks. Their complex 3D design and their history of worse confinement than tokamaks led them to be superseded by tokamaks. The optimization made possible by advances in computing and improvements in plasma theory has lead to stellarators with better confinement properties.

This has led to an increased interest in stellarators worldwide, especially as this coincided with the recognition of the seriousness of the issues facing the tokamak concept.

## 1.1 The Helically Symmetric eXperiment

The stellarator was invented by Lyman Spitzer in 1952. Stellarators are designed such that the magnetic field that confines the plasma is created by the magnetic coils. This separates them from tokamaks where some of the magnetic field is from large currents in the plasma. The Helically Symmetric eXperiment (HSX) is a quasi-symmetric stellarator. The quasi-symmetric configuration possess a direction of symmetry in magnetic field strength and this allows a stellarator to have good particle confinement at low collisionality, like a tokamak, by reducing the neoclassical transport. Transport in the QHS configuration has been shown to be significantly reduced in comparison to a configurations where the symmetry was intentionally degraded [1]. Typical plasma parameters for HSX in plasmas with methane as a fill gas are shown in figure 1.2.

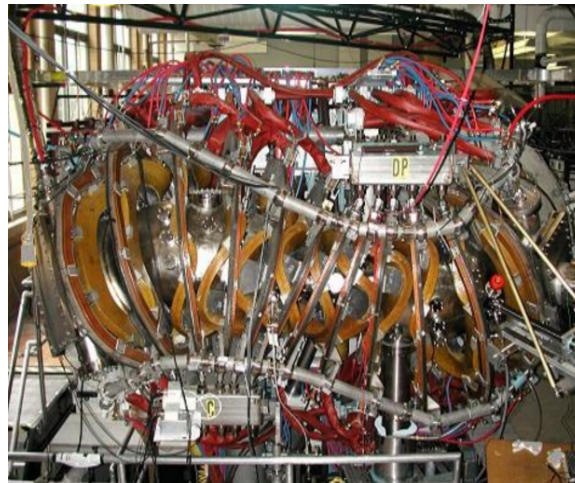


**Figure 1.1 HSX Stellarator** A field period of the HSX device is shown. The plasma confinement in HSX was optimized to reduce neoclassical transport through a symmetry direction in magnetic field strength.

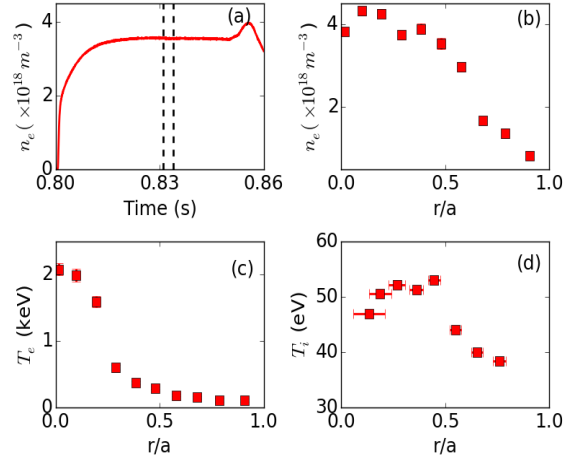


**Figure 1.2 HSX plasma Parameters** The plasma parameters of 100 kW methane plasmas in the standard configuration are shown. These are the hottest plasmas achievable on HSX. The line averaged density and beam fire time are plotted in the top left. The Thompson scattering temperature and density. The Carbon ion temperature was measured with the CHERS system.

## 1.2 The Importance of $E_r$ on Stellarators

The radial electric field has important effects on transport and plasma flows in stellarators. For example, it can affect the neoclassical heat, particle, and impurity transport. The neoclassical transport in the  $1/\nu$  low collisionality regime (the relevant regime for a reactor) is greatly reduced by the presence of a radial electric field [2] (see figure 1.3). Without the presence of a radial electric field the scaling of stellarators in the low collisionality regime is [3]:

$$D_{\frac{1}{\nu}}^* \propto \epsilon_{eff}^{\frac{3}{2}} \frac{T^{\frac{7}{2}}}{n} \quad (1.1)$$

This scaling has the potential make the stellarator unworkable as a reactor, where the temperatures are expected to be higher than in current experiments. In HSX,  $\epsilon_{eff}$  is much lower than other stellarators [3], which reduces the neoclassical transport relative to these other devices, but the temperature dependence is still problematic. The addition of an electric field can further reduce the

transport in the low collisionality regime, as seen in figure 1.3 to make the neoclassical transport scale more like that of a tokamak.

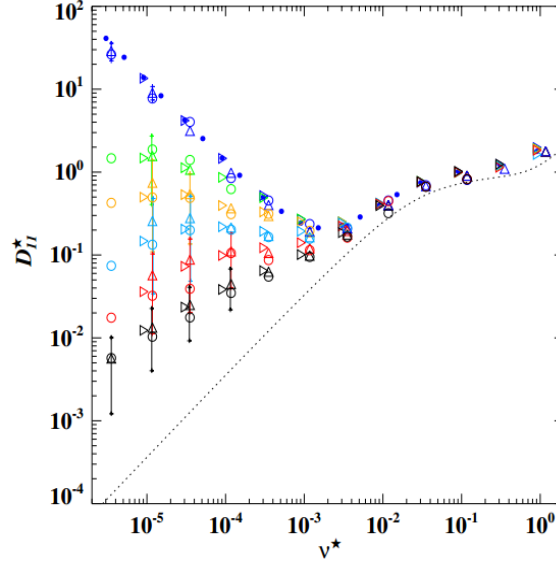


**Figure 1.3 Transport changes with  $E_r$**  The normalized mono-energetic radial transport coefficients as a function of collisionality for HSX are plotted. As  $E_r$  increased the transport is reduced in the low collisionality regime. An equivalent tokamak is the dashed line, and with a sufficient electric field the transport begins to scale like the tokamak, though starting from a higher value. The results were calculated with the NEO-2, DKES, and a Monte Carlo code. The figure is reproduced from [4].

In addition, a positive electric field can lead to impurity expulsion from the core [5, 6] which is advantageous for core plasma performance. The radial electric field can also effect the magnitude of the bootstrap current [7]. For example, on HSX switching between the ion and electron roots (the low and high electric field cases) was calculated to reverse the direction of the bootstrap current in the core [8]. The change in bootstrap current can in turn have important effects on the magnetic topology. This is important because it can affect the location of the strike-points on the divertor.

### 1.3 Outline of Thesis Work

The following section will outline the remainder of this thesis. Chapter 2 will cover the theory behind the flow and radial electric fields on stellarators. In addition, a review of previous results of flow and  $E_r$  on HSX and other stellarators will be presented.

Chapter 3 will discuss the Pfirsch-Schlüter CHERS system, the theory behind the diagnostic and experimental setup. The Pfirsch-Schlüter CHERS system measures the flow on the inboard and outboard side of HSX in order to measure the counter streaming Pfirsch-Schlüter component of the impurity ion flow. These measurements of Pfirsch-Schlüter flow can then be used to calculate  $E_r$  and the bootstrap flow and offer an alternative to the force balance method to measure the radial electric field in the plasma[9]. In addition to measuring the Pfirsch-Schlüter component of the impurity ion flow, the system also measures the bootstrap component of the impurity ion flow. This has been used to simultaneously measure the electric field and flow profile evolution of the plasma throughout the discharge. Passive spectroscopy has also been used for flow evolution measurements.

The chapter also it will discuss the synthetic diagnostic developed to compare the results to theoretical calculations. In order to properly compare the measurements from the CHERS system to PENTA calculations, a synthetic diagnostic has been developed. This is important because the measurements of both systems cannot be accurately approximated as a point measurement, due to the relatively large beam width and finite spot sizes of the view. Some of the quantities of interest vary by as much as 50% between the focal point and sightline averaged values. The effect of the beam and plasma density, beam width, electric field profile, and magnetic field direction were included into the model to directly compare the measurements to the PENTA calculations[10].

Chapter 4 will present the results of the Pfirsch-Schlüter measurements of flow and  $E_r$  will be presented. Finally, conclusions and future work will be discussed in chapter 5.

## References

1. Canik, J. M. *et al.* Experimental Demonstration of Improved Neoclassical Transport with Quasihelical Symmetry. *Phys. Rev. Lett.* **98**.
2. Mynick, H. & Hitchon, W. Effect of the ambipolar potential on stellarator confinement. *Nuclear Fusion* **23**, 1053 (1983).
3. Mynick, H. E. Verification of the classical theory of helical transport in stellarators. *Physics of Fluids* **25** (1982).
4. Beidler, C. *et al.* Benchmarking of the mono-energetic transport coefficients results from the International Collaboration on Neoclassical Transport in Stellarators (ICNTS). *Nuclear Fusion* **51**, 076001 (2011).
5. Burhenn, R. *et al.* On impurity handling in high performance stellarator/heliotron plasmas. *Nuclear Fusion* **49**, 065005 (2009).
6. Nakamura, Y *et al.* Impurity shielding criteria for steady state hydrogen plasmas in the LHD, a heliotron-type device. *Plasma Physics and Controlled Fusion* **56**, 075014 (2014).
7. Watanabe, K. *et al.* Effect of collisionality and radial electric field on bootstrap current in the Large Helical Device. *Nuclear Fusion* **35**, 335 (1995).
8. Schmitt, J. C., Talmadge, J. N., Anderson, D. T. & Hanson, J. D. Modeling, measurement, and 3-D equilibrium reconstruction of the bootstrap current in the Helically Symmetric Experiment. *Physics of Plasmas* **21** (2014).
9. Kumar, S. T. A. *et al.* Determination of radial electric field from Pfirsch-Schluter flows in the HSX stellarator. *Nuclear Fusion* (accepted 2016).

10. Dobbins, T. J., Kumar, S. T. A. & Anderson, D. T. A synthetic diagnostic for beam emission spectroscopy in the helically symmetric experiment stellarator. *Review of Scientific Instruments* **87** (2016).





$$m_i n_i \frac{\partial V_i}{\partial t} + m_i n_i V_i \cdot \nabla V_i = e n_i (E + V_i \times B) - \nabla p_i - \nabla \cdot \bar{\pi} + F_i - m_i N_i \nu_{in} V_i \quad (2.1)$$

and the continuity equation is given by:

$$\frac{\partial n_i}{\partial t} + \nabla \cdot n_i V_i = 0 \quad (2.2)$$

[12] where  $V_i$  is the ion velocity,  $m_i$  is the ion mass,  $n_i$  is the ion density,  $E$  is the radial electric field,  $B$  is the magnetic field,  $p_i$  is the pressure given by  $n_i T_i$ ,  $\bar{\pi}$  is the viscosity tensor,  $F_i$  is the friction force between ions and electrons ( $F_i = m_i n_i \nu_{ie} (V_e - V_i) = -F_e$ ) and can also be used for any external momentum sources, and  $m_i N_i \nu_{in} V_i$  is the drag from neutral collisions. By solving these equations, the flows can be calculated for a plasma device.

The electron momentum balance is similar to the ion equations and by using both the electron and ion(s) equations, the flows can be solved for. This can be done analytically in some plasmas parameters found on HSX or by using neoclassical codes like PENTA[13, 14], though each of these models leaves out important factors for flows in HSX. These models will be described in this section.

## 2.1 Neoclassical flows and $E_r$ in Stellarators

Unlike in tokamaks, which are intrinsically ambipolar (the ion and electron charge flux are always equal), stellarators typically require an electric field to develop in order to achieve ambipolarity. In the absence of externally injected momentum, the radial electric field of stellarators typically arises as a result of the non-ambipolar component of the radial particle flux. That flux leads to a charge imbalance in the plasma and thereby an electric field. The electric field will evolve until a charge flux balance is reached, giving fluxes of the species the following form  $Z_{eff} \Gamma_i = \Gamma_e$ . The relationship between the fluxes of ions and electrons as a function of the radial electric field is not linear, however (see figure 2.2). Therefore, the fluxes of ions and electrons as a function

of radial electric field are calculated. The points of intersection of the two fluxes give the possible  $E_r$  values that achieve ambipolar fluxes (there can be more than one solution). This calculation is performed for HSX using the PENTA neoclassical code [13, 14]. PENTA also allows for the calculation of ion and electron flow (and from those plasma current) by including momentum correction to the DKES code [13, 14]. It calculates the relationship between the radial electric field and bootstrap flow on a flux surface and then uses the calculated ambipolar root(s) to find the plasma flow. Figures ?? show the PENTA calculation for bootstrap flow as a function of radial electric field. The calculated values of plasma flow, current, and flux have been previously compared to experimental measurements of flow, transport,  $E_r$ , and bootstrap current[8, 15, 16] on HSX, as will be described presently.

Other devices to show it can work, W7AS, etc. see Alexis's review or other reviews, include plots

There are two stable roots typically found in most HSX plasmas, called the electron and ion roots. On most devices, the ion root is typically at a negative electric field, but on HSX it is a small positive electric field due to the low  $T_i$  relative to  $T_e$  (a similar result was seen on W7AS [17]). The electron root has a larger positive electric field and lower levels of transport relative to the ion root case. The electron root's lower transport would allow for larger gradients and more peaked profiles. This effect has been measured on LHD[18] and W7AS [19]. PENTA predicts only an ion root in the edge of HSX but either both roots or just the electron root in the core of most HSX plasmas[8].

In a traditional stellarator, there are large neoclassical viscous damping of flows in all directions due to the complex variation of  $|B|$  on a flux surface and the radial electric field is set by the ambipolar constraint mentioned above. This results in the flows to be set neoclassically, at least in the absence of large external flow drives. For example, the perpendicular flows are proportional to the radial electric field (from the  $E \times B$  flows), which in turn is set by the ambipolarity constraint

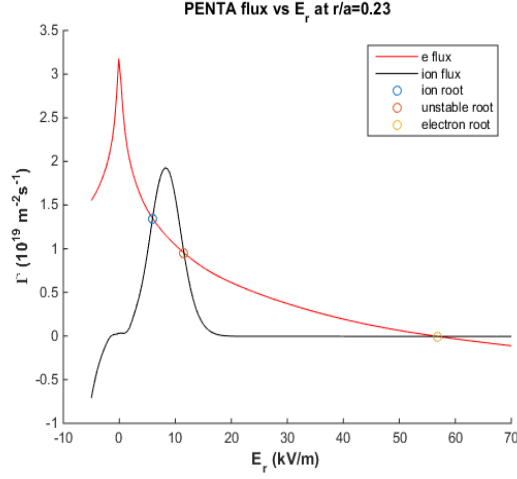


**Figure 2.2 Radial Particle Fluxes from PENTA** The ion and electron fluxes as a function of  $E_r$  are calculated by PENTA for a typical QHS plasma. There are three locations where the fluxes are equal, but only two of the roots are stable. The two stable roots are the electron and ion roots. The peaks in the ion flux are from the helical resonance.

mentioned above. The bootstrap flow is then a result of the neoclassical viscosity described in equation 2.1, that couples the perpendicular and parallel flows.

The direction of the intrinsic flow was seen to be due to the dominate ripple term in LHD [LHD flow direction and ripple], where the direction of flow reversed between the core and the edge as ratio of the toroidal and helical ripple changed. In CTH flow is also seen to progress in the direction of minimum gradient of  $B$  (and thereby the direction of lowest flow damping)[20]. This is similar to the case in HSX where flow is expected in the symmetry, or minimum gradient of  $B$  direction, though the amount of damping in the symmetry direction in HSX should be much lower than CTH.

On a quasi-symmetric stellarator, the picture is different from the traditional stellarator. HSX was designed to reduce neoclassical transport through quasi-symmetry, though the quasi symmetry is not perfect on HSX). Quasi-symmetry arises when there is a direction of symmetry in the magnetic field strength, more specifically, the Fourier spectrum of  $|B|$  on a magnetic surface is

dominated by a specific harmonic (the  $(n,m)=(4,1)$  mode for HSX). This symmetry removes many of the ‘direct loss’ orbits found in unoptimized stellarators, greatly reducing neoclassical transport. The optimization allows for many of the neoclassical properties of HSX to become tokamak like. For example, a quasi-symmetric stellarator is intrinsically ambipolar (and therefore the radial electric field is not set by neoclassical transport, but by other factors like Reynolds stress). In addition, it can have free flowing flow in the symmetry direction[21], while the flow in the asymmetric direction will be damped. This is similar to a tokamak where, due to axisymmetry, the toroidal flow is not damped but the poloidal flow is (see figure 2.4).

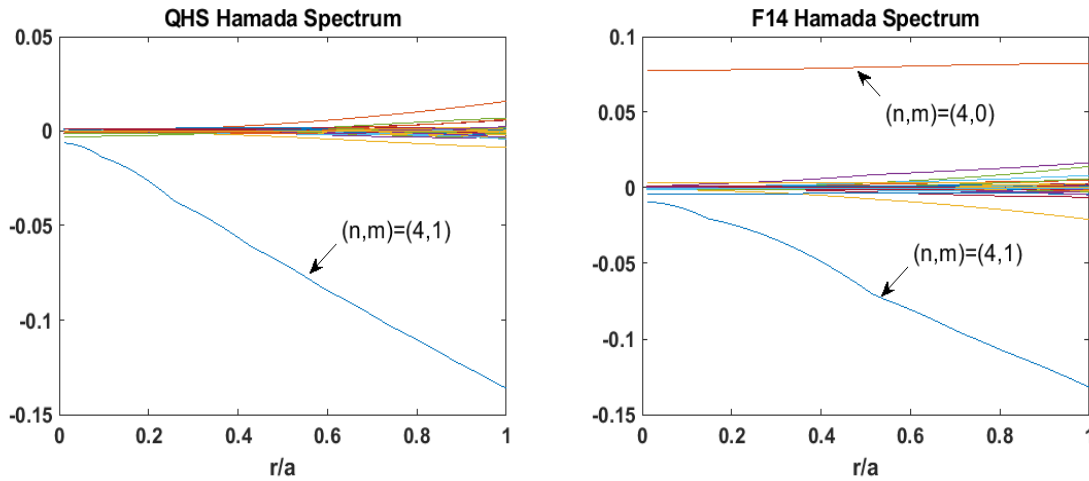


**Figure 2.3 Hamada Spectrum of HSX in QHS and F14.** The symmetry is broken in F14 by including a large 4,0 mode, while in QHS the spectrum is dominated by the 4,1 mode across the minor radius.

No real device is perfectly quasi-symmetric, however. For example, the quasi-symmetry in HSX is not perfect due to other modes that appear in the magnetic spectrum from things like coil ripple. The Hamada spectrum of HSX in the QHS and F14 configurations (symmetric and symmetry broken cases respectively) are shown in figure 2.3 and show the quality of the quasi-symmetry [22, 23]. It is an open question to determine how close an experiment has to be to quasi-symmetry

to get the benefits associated with quasi-symmetry. This is thought to be dependent on what parameter you are looking at (flow damping, fast ion confinement, reduction of direct loss orbits, etc.). This has been studied in the past by intentionally breaking the symmetry of the device with auxiliary coils to add additional modes to the magnetic spectrum and raise the effective ripple in the plasma, as described briefly in chapter one. As shown in the PENTA calculations in figure 2.2, the symmetry breaking in QHS is enough to make the neoclassical transport nonambipolar. This would suggest that the radial electric field will be set by neoclassical effects. However, if the neoclassical nonambipolar flux is small enough, the radial current from Reynolds stress could dominate or compete with the neoclassical fluxes to set the radial electric field and maintain quasineutrality. This will be examined further in section 2.3.3.

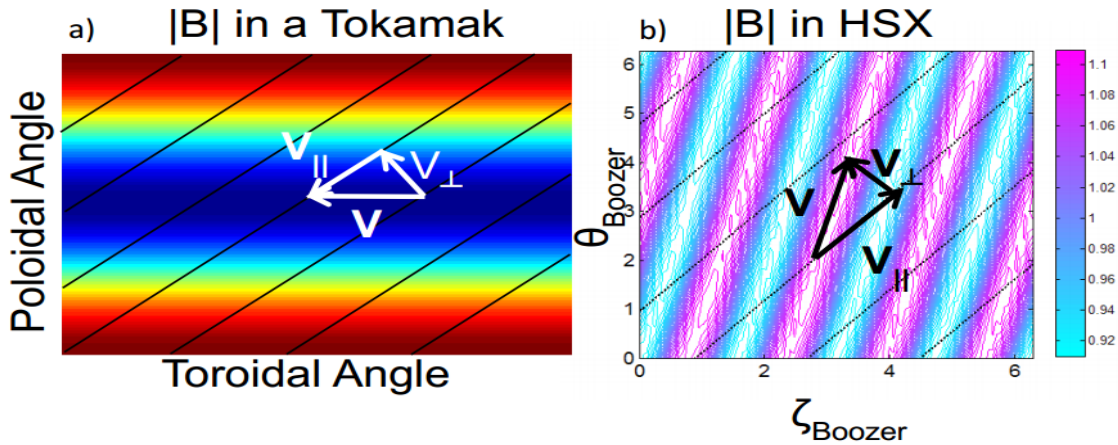


**Figure 2.4** The magnetic field contours relationship to flow direction for a tokamak and HSX. Both configurations have flows that can flow in the direction of magnetic field strength, by having a balance of parallel and perpendicular flow. Note that the flow direction is in the opposite direction in QHS for the same direction of perpendicular flow as a tokamak. Figure reproduced from [15]

The symmetry direction is the direction with lowest flow damping, so it is intuitively expected that the intrinsic plasma flow is in the symmetry direction in HSX. Previous CHERS measurements showed that the flow was near the symmetry direction [15] on HSX. The symmetry direction in

HSX is not identical to the parallel direction, though it is very close to it in the core and only  $\sim 15^\circ$  away in the edge. Therefore, for the flow to propagate in the symmetry direction there needs to be a balance of  $v_{\parallel}$  and  $v_{\perp}$  (see figure 2.4 for an example). Due to the fact that perpendicular flow is related to the radial electric field, there is a ratio between the bootstrap flow and radial electric field needed to have flows in the symmetry direction. This relationship can be calculated using the Hamada spectrum, and has been described in depth previously [15]. The result, in terms of the output of PENTA is as follows:

$$\frac{\langle V_{\parallel} B \rangle}{B^2} = C_{sym} \left( E_{r,PENTA} - \frac{1}{en_i Z_i} \frac{\partial p_i}{\partial r_{PENTA}} \right) \quad (2.3)$$

where

$$C_{sym} \equiv \frac{2\pi^2 \sqrt{g}}{4 - \iota} \sqrt{\frac{1}{\partial r_{PENTA}}} \quad (2.4)$$

[15]

These equations can then be compared to the predicted flow vs radial electric field predicted by PENTA. When that is done, it is found that at small values of radial electric field, PENTA predicts the flow to be in the symmetry direction (as can be seen in figure 2.5). Analytic neoclassical theory also agrees with this conclusion as will be discussed in section ... .

There are several deviations from the symmetry direction predicted by PENTA, however, that can be seen in figure 2.5 and each will be discussed in their turn. First, there is an offset of flow in the parallel direction arising from the finite plasma current. Secondly, at small radii in QHS and across the radius of F14 the flow direction predicted by PENTA deviates from the symmetry direction. This occurs due to the occurrence of other modes besides the 1,4 mode that damp flow in the symmetry direction (see figure 2.3). In HSX, the symmetric mode is the dominate mode across the entire minor radius, though its relative strength is peaked in the midradius and weakest in the core. In F14, the symmetry breaking (4,0) is the dominate mode for much of the plasma radii

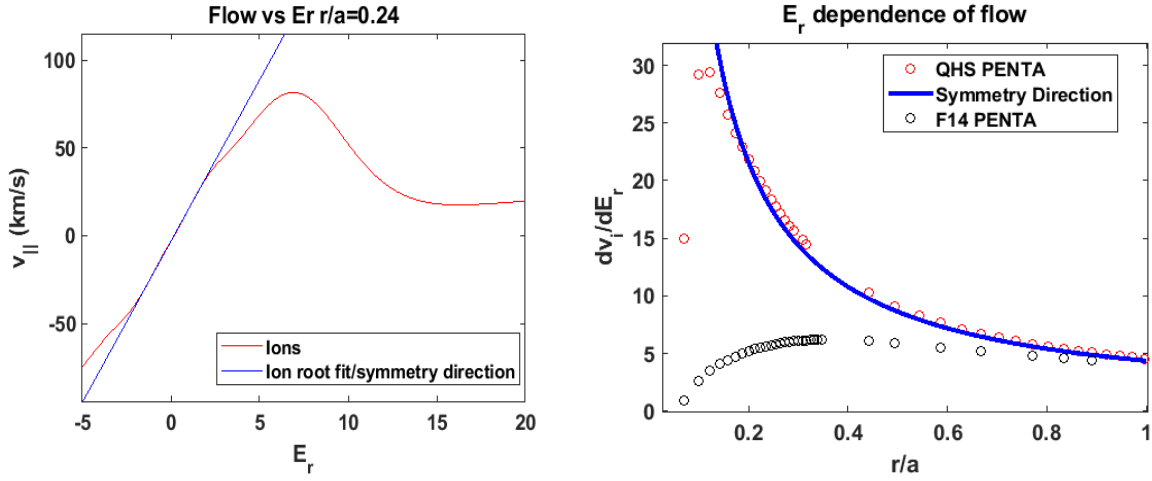


**Figure 2.5** The flow direction predicted by PENTA compared to the symmetry direction on HSX. The flow predicted by PENTA at low values of radial electric field is fit to find the dependence of flow on radial electric field. The dependence calculated by PENTA is in the direction of symmetry except for in the very core of the plasma and in F14. The deviation arises due to the relative importance of the symmetry breaking terms in the core of QHS and across the plasma in F14.

(see figure 2.6). The deviation from the symmetry direction effect is seen to be dependent on the collisionality regime by scanning the temperature of the ions and electrons inputted into PENTA. As the ions and electrons decrease in collisionality the deviation is calculated to increase. This occurs because at low collisionality the particles ‘see’ the magnetic ripple more and are thereby more effected by the deviations from quasisymmetry on HSX.

Finally, in the region of the helical resonance (and radial electric fields beyond the resonance) flows are predicted to flow in non-symmetric directions. This deviation will be described after the resonance is explained in section 2.1.1.

### 2.1.1 The Helical Resonance

The particle resonance plays an important role in the neoclassical transport calculations on HSX. They arise because of the change in particle trajectories caused by the  $E \times B$  drift. The resonance can be understood much more easily in the tokamak case, so they will be described



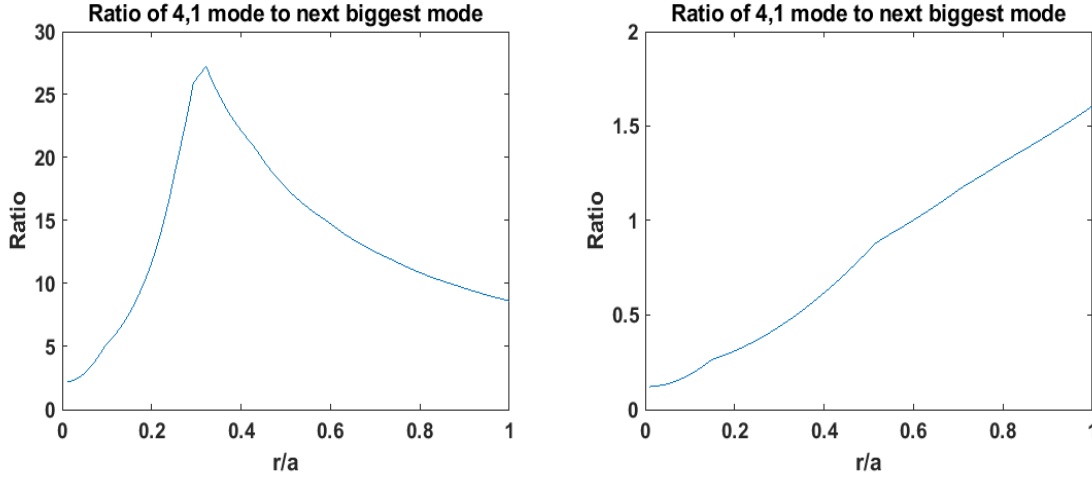


**Figure 2.6 Ratio of the symmetric (4,1) mode to next largest mode in QHS and F14.** In HSX, the symmetric mode is the dominate mode across the minor radius, though its relative strength is peaked in the midradius and weakest in the core. In F14, the symmetry breaking (4,0) is the dominate mode for much of the plasma radii. Note, all of the modes matter to the flow dampening, not just the largest two modes, especially in QHS where many of the sub-dominant modes are of the same order.

there first. In a tokamak, if a particle has a purely toroidal trajectory, then the particle experiences vertical  $\nabla B$  and curvature drifts and will quickly leave the plasma volume. This is the reason why a poloidal magnetic field is needed for confinement in a tokamak. The procession of the particle in the poloidal direction makes the net vertical drift average to zero. Purely toroidal flow can be recovered when a balance of  $v_{||}$  and  $E \times B$  flow is reached (see figure 2.7). At this point, the vertical drift would return. This can also be thought of is that at the resonance it is equivalent to having the rotation transform equal to zero.

In stellarators there are many more magnetic modes than in a tokamak, each of which can have a resonance, because each contribute to the  $\nabla B$  and curvature drifts. If the ratio of the toroidal and poloidal angular velocities of a particle ( $\omega_{\zeta}$  and  $\omega_{\theta}$  respectively) is  $\frac{\omega_{\zeta}}{\omega_{\theta}} = \frac{m}{n}$ , where m and n are the mode numbers of a mode in the magnetic spectrum, then the particle will experience an uncompensated vertical drift. By converting the angular velocities into parallel velocities and radial electric fields the relationship between the radial electric field resonance can be found.

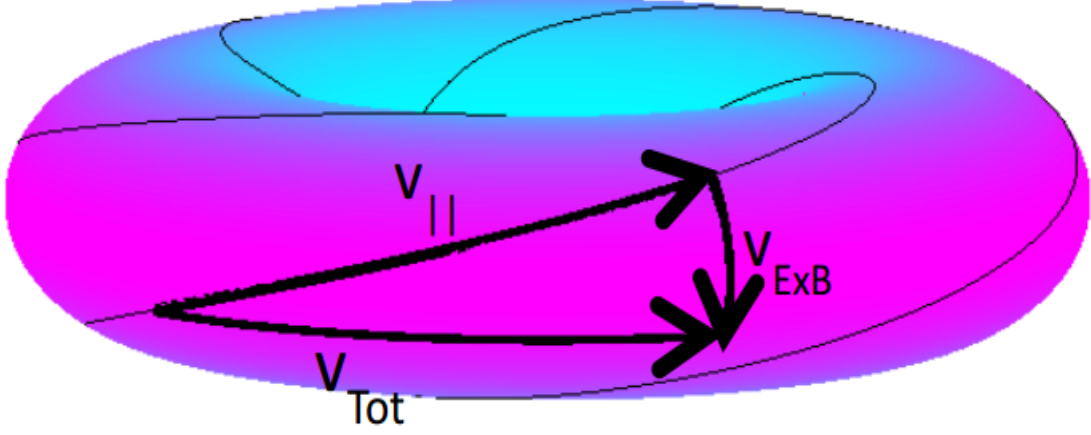


**Figure 2.7 The tokamak particle resonance.** Purely toroidal flow can be achieved when a balance of  $v_{||}$  and  $E \times B$ . At this point (the resonance) there is an uncompensated vertical drift of the resonant particle.  
Figure reproduced from [15]

$$E_r = \frac{(m - \frac{nr}{R} \frac{B_z}{B_\theta}) B_\theta}{m \frac{B_z}{|B|}} v_{||} \cong \frac{(m - \frac{n}{i}) B_\theta}{m} v_{||} \quad (2.5)$$

Due to the helical nature of the resonance on HSX, seen in the equation above, is that the  $E \times B$  needed to reach the resonance is 3 times bigger than an equivalent tokamak[15]. To find the rate of particle flux due to the resonance, it is first necessary to find the population of particles at or near the resonance. When the plasma velocity is much smaller than the thermal velocity (this assumption will be examined presently), then the plasma can be assumed to be Maxwellian, and the number of particles at any given  $v_{||}$  will be proportional to  $e^{-\frac{v_{||}^2}{v_{th}^2}}$ . The rate of particle loss of the plasma due to the resonance is proportional to the drift velocity. The drift radially in turn is proportional to  $v_{||}^2$  [24]. By combining these effects, the flux from the resonance is given by  $v_{||}^2 e^{-\frac{v_{||}^2}{v_{th}^2}}$ . This function has peaks around where  $v_{||} = \pm v_{th}$ . Note, the particle distribution function will no longer be well described by a Maxwellian at this point, but the general trend holds. This resonance in ion particle flux can be seen in figure 2.2, where the flux increases up to the resonance and then

decreases at radial electric fields above the resonance, (though the PENTA code breaks down at the resonance it does show the proper trend). The resulting radial electric field at the resonance is

$$E_r = \frac{(m - \frac{n}{l})B_\theta}{m}v_{th} \quad (2.6)$$

This equation shows that the resonance can be increased to larger values of radial electric field by increasing the magnetic field of the device, changing the mode number of the direction of symmetry, changing the mass of the plasma particles, or raising the temperature of the device. The first two can only be done in the design phase of the experiment, while raising the temperature increases the resonance as  $T^{\frac{1}{2}}$ . Due to the  $v_{||}^2$  dependence of the flux, as the temperature increases the flux increases and the region of significant flux from the resonance broadens. The broadening of the resonance with an increase in temperature results in the flux at the old resonance radial electric field to remain fairly constant, as was previously seen in PENTA parameter scans [15]. The value of the radial electric field at the resonance will tend to decrease towards the core due to the decrease in  $B_\theta$  in the core (though this can be partially balanced out by the temperature increase in the core).

Another way to think about the resonance condition is that it corresponds to the value of radial electric field above which the banana orbits associated with a magnetic mode  $m,n$  disappear ?? . The dominance of the 4,1 mode in HSX compared to the other modes, and the larger number of particles in banana orbits trapped by this mode is the reason why PENTA results are dominated by only the helical resonance in QHS plasmas. This can also affect the relative strength of the resonance in HSX compared to other stellarators with a multitude of modes, each with their own, relatively smaller, resonances. The strength of the resonance is also most pronounced in the low collisionality regime, but still can be significant in higher collisionality regimes, like those in HSX.

The computations of the neoclassical codes DKES and thereby PENTA, which relies on DKES, breaks down near the resonance due to the mono-energetic assumption[13, 14] of DKES. The

inaccuracy arises from DKES assumption  $\vec{v}_E = \frac{\vec{E} \times \vec{B}}{B^2} \sim \frac{\vec{E} \times \vec{B}}{\langle B^2 \rangle}$ . There is typically a small difference between  $\frac{\vec{E} \times \vec{B}}{B^2}$  and  $\frac{\vec{E} \times \vec{B}}{\langle B^2 \rangle}$ , but there is a nonphysical singularity at the resonance[25]. Comparisons to codes that take this properly into account show that DKES showed good agreement when  $E_r$  is below  $\frac{E_r^{res}}{2}$  and above  $2E_r^{res}$ [26].

### 2.1.2 Electron Root Plasmas

In addition, the validity of using the mono-energetic approximation assumed by PENTA can be inaccurate in HSX away from the resonance [27, 28]. This violation arises from the fact that a finite electric field will effect the particle orbit itself. This is clear when the change in energy from the electric field over a gyro orbit is a significant fraction of (or larger than) the ion temperature. The ion gyro-radii are  $r_{H^+} \sim 1$  mm for hydrogen ions and  $r_{C^{+6}} \sim 0.5$  mm for fully stripped carbon ions (assuming that they have the same temperature). An unperturbed orbit will see a potential of  $\Delta\phi = 2E_r r_{gyro}$ . The change in energy from this potential is equal to the charge times the potential,  $Z \Delta\phi$ . With a large electric field the change in energy can be a significant portion of or even larger than the thermal energy. The ion temperature is 60 eV in the core. In the core a 28 kV/m radial electric field will lead to an energy shift equal to the hydrogen thermal energy and a 9 kV/m field will do so for fully stripped carbon ions. The electric field calculated by PENTA in the core is 40-60 kV/m and around 5 kV/m in the edge, depending on the configuration. These fields would violate the mono-energetic assumption of PENTA. The measured field of approximately 5-10 kV/m was lower than the PENTA calculation however, but not low enough for the carbon to be mono-energetic[15].

The effect of the finite electric field also changes the population of trapped particles differently than DKES predicts[27] due to errors in calculating the trajectories using DKES. While both cases have the trapped particle fraction decreasing as  $e^{-(\frac{E_r}{E_r^{res}})^2}$ , DKES leaves out additional terms dependent on the radial electric field. The under-prediction of the trapped particle fraction is about

a factor of two at the resonance and around 70% at twice the resonance. This result may lead to DKES, and thereby PENTA, to dramatically misrepresent the neoclassical ion transport in the electron root regime of HSX which can have the radial electric field much larger than the resonance.

W7AS, in their electron root plasmas and taking into account the ECRH driven flux, concluded that another effect may lead to the underestimation of the radial flux of ions at large radial electric fields. They claimed that the traditional neoclassical assumption in the drift kinetic equation that the ‘parallel’ mirror term  $\propto (v/B^2)B \cdot \nabla B$ , is large compared to the ‘poloidal’ mirror term  $\propto (p/B^3)(E_r \times B) \cdot \nabla B$ , may be violated under the electron root condition for the ions (but not the electrons)[19]. Their results will be discussed more in the ECRH driven flux section.

These factors leading to more ion flux at high radial electric fields may not be important on HSX however. First, the radial electric fields measured experimentally have always been small, at ion root levels. While the electric field can approach the resonance value experimentally, the electric field is not at the high levels predicted by the electron root. Secondly, the electron flux dependence on  $E_r$  is calculated to be much, much stronger ion dependence by PENTA in the electron root region, and the increases from the causes mentioned above may not be high enough to balance this out (see figure 2.2).

First at low levels of radial electric field the flow is calculated to flow in the symmetry direction. Once, the ion resonance is

Importance of flow and flow shear for turbulence vs driving flux from the resonance if have high flow

There are several important things to note in the plot.

Once  $E_r$  is know, how does this effect flows, coupling between  $v_{\text{perp}}$  and  $v_{\text{par}}$  More Neoclassical theory relating to  $E_r$  and flows Force balance equation

Diffusion of  $E_r$

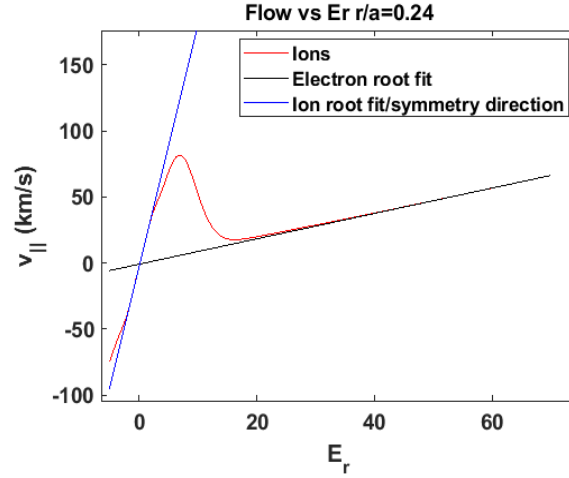


**Figure 2.8 Flows vs  $E_r$  from PENTA** The flows as a function of radial electric field are plotted. At small radial electric field, the flow is in the symmetry direction, but after the resonance the flow no longer propagated in the symmetry direction.

## 2.2 Analytic Neoclassical theory for Flows in Stellarators

flow vs  $E_r$  dependence in PENTA and analytic theory plot (more in later sections?) in QHS and F14

deviation from symmetry direction and boozer spectrum and temperature

quasi-symmetry and NC Mach number and Quasi symmetry breaking: With a finite plasma velocity, perfect quasi-symmetry is broken due to potential variations on a flux surface caused by the flow. The breaking scales like  $M^4 \epsilon^{7/2} / \nu_e$  for electrons. This means that the  $1/\nu$  regime returns even in perfect quasi-symmetry with flows[29]. That being said, perfect quasi-symmetry is impossible in any real machine[30], so the question then becomes how this scales compared to the neoclassical flux from a real device. This flux is expected to be weak compared to the as built device because  $M$  and  $\epsilon$  are expected to be small ( $\epsilon \sim 1/10$  in HSX)[29]. If the flow was very large however, it could become comparable to the as built neoclassical flux.

flow damping by configuration in HSX and elsewhere resonance

## 2.3 Non-Neoclassical flows and $E_r$ in optimized Stellarators

There are several other contributors to flows and radial electric field in fusion plasmas besides the neoclassical radial electric field [11]. The most common external driver of flows in plasmas are neutral beams, but HSX does not have a beam able to drive flows. More relevant factors include ECRH driven electron flux, neutral and charge exchange drag forces, and turbulent driven flows and these will be described below.

### 2.3.1 ECRH driven torque

add stuff about profile of  $E_r$  dependence, W7AS paper on electron root and underestimating ion flux at high  $E_r$

The ECRH heating system is calculated to drive an electron flux on HSX. This current will lead to the development of an electric field, which in turn will drive flows, similarly to the neoclassical fluxes described before. To calculate the magnitude of this effect, the GNET code[cite] was used to calculate the electron flux and corresponding torque on the plasma in QHS and F14. The results on QHS showed the levels of electron flux were comparable to PENTA electron fluxes and in F14 the fluxes were higher than the neoclassical values (see figure 2.9).

The calculated fluxes from ECRH are dependent on the radial electric field however, so a self consistent calculation combining the neoclassical and ECRH driven flux would be needed to properly calculate this effect. As such, preliminary calculations were done to combine GNET with PENTA to get a self-consistent radial electric field value [cite]. The results suggest that in QHS the increase in electron flux lead to a small increase in  $E_r$  in the ion root only region and a large increase in the electron root only regime. This is because of the different dependency on a change of electron flux to the ambipolar root on the electron root vs the ion root solutions. In calculations in F14 the effect of the ECRH system was much larger due to the higher ripple. The electron flux

is calculated to be higher than the PENTA prediction for the electron flux by as much as a factor of 10. This is expected to significantly effect the radial electric field and flow. It should be noted that there was no self-consistent calculation done for F14 however and a dramatically higher electric field was not seen in the measurements in this thesis.

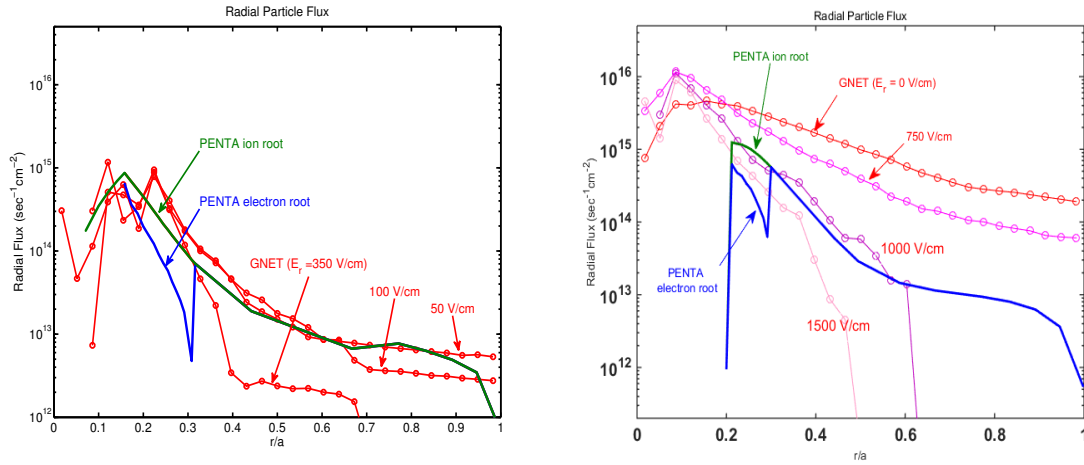


**Figure 2.9 ECRH flux calculated by GNET.** The flux of electrons from PENTA and from GNET at different values of radial electric field are plotted for QHS on the left and F14 on the right. On QHS the electron flux is comparable to the neoclassical values, while for experimentally relevant electric fields the ECRH flux is higher than the neoclassical flux.

The torque from this flux was also calculated for QHS and F14 and the result of the calculation can be seen in figure 2.10. The torque was larger and more broad in F14 than in QHS[31]. This could help explain the higher flow seen in F14 (see figure...) compared to QHS despite the higher dampening. The torque arises from two effects from the heating. First, the radial current driven by the ECRH system drives a  $\mathbf{J} \times \mathbf{B}$  torque and secondly the friction of the precession motion of the supra-thermal electrons with the plasma can cause a collisional torque on the plasma. The magnitude of these terms on HSX can be seen in figure 2.10.



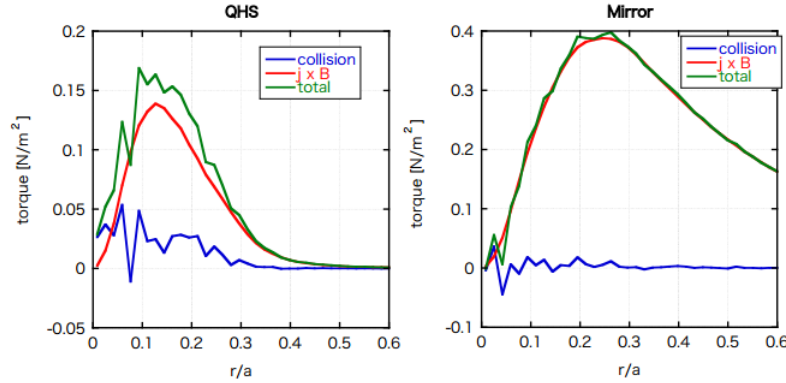


**Figure 2.10 ECRH torque calculated by GNET.** The torque driven by ECRH heating is much higher and broader in F14 than in QHS. This flux is primarily a result of the electron flux driven by the ECRH system.

### 2.3.2 Neutral dampening

add tokamak neutral effects,  $10^{-3}$  and  $10^{-4}$  when neutrals matter and when effect ion distribution.  $E_r$  from neutrals

ratio of HSX neutrals and plasma

neutrals and flow direction using analytic theory combine reduction factor with PENTA

Neutrals can penetrate into the core of HSX and these neutrals will provide a drag force on the ions. The ion temperature and neutral density are not changed significantly between configurations, so this damping should be configuration independent. A simple estimate of the ion-neutral collision frequency from Cornrlis et al.[32],  $\nu_{in} \approx N_n 10^{-8} T_i^{.318}$ , gives a reasonable estimate of the loss of momentum from ion neutral friction [33].

Another effect of neutrals on flow comes from charge exchange dampening. Charge exchange leads to a non-ambipolar current the opposes the electric field direction. This would have the effect of decreasing the value of flow and  $E_r$  relative to the values predicted by PENTA. This effect could be important on HSX due to neutral penetration into the HSX core, however at the ion temperatures

at HSX the charge exchange cross section is much lower than the neutral dampening (see figure 2.11) [34].

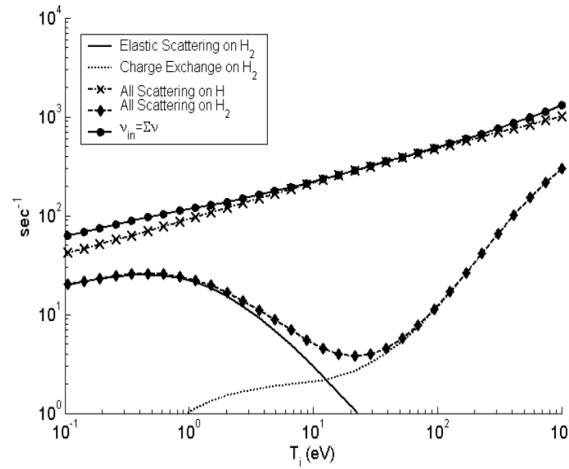


**Figure 2.11 Neutral dampening rates** The neutral dampening and the charge exchange from H and H<sub>2</sub> gas are shown. The figure is from [34].

By using the modeled neutral density and measured ion temperature the dampening rate can be found. This dampening can be a significant compared to the neoclassical dampening rates (see figure 2.12). The neoclassical rates were calculated in the direction of symmetry (the slow rate) and perpendicular to the direction of symmetry (fast rate). Only the dampening in the symmetry direction in QHS is smaller than the calculated neutral dampening. In the core the neutral dampening is larger than the neoclassical dampening by almost a factor of 10. This suggests that the flow predicted by a neoclassical code that ignores neutral friction will probably be inaccurate for flows in the symmetry direction in QHS, but potentially more accurate in other configurations where this effect is smaller.

In the edge the dampening rates were compared to the neoclassical calculations by using a bias probe to measure the flow. The dampening was significantly higher (5-10 times larger) than the neoclassical values, but the difference in dampening between QHS and F14 was comparable to

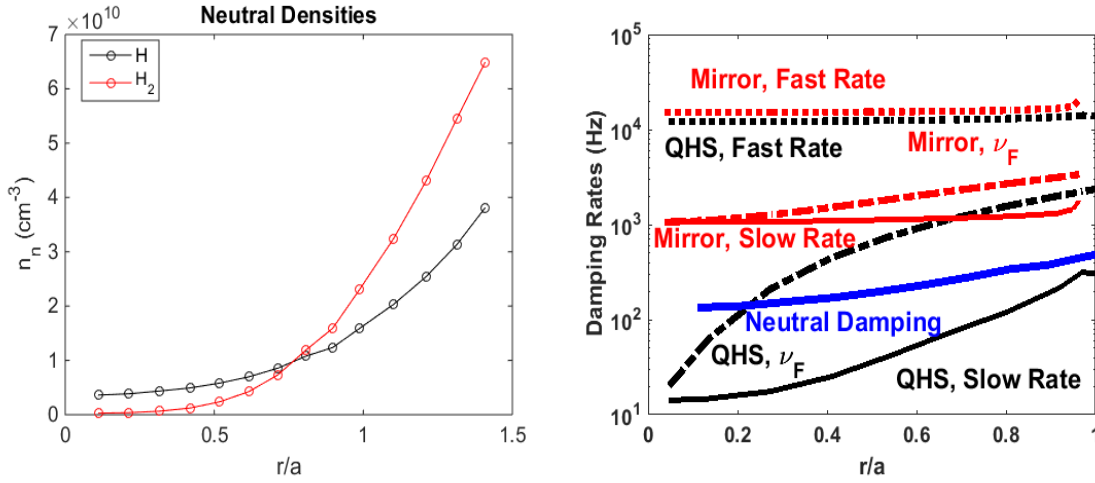


**Figure 2.12 Neutral density and damping on HSX.** The neutral density on HSX is plotted on the left. It is peaked in the edge, but a significant population can be found in the core. The first plot is courtesy of L. Stephey. The second figure was taken from [33] and the neutral damping was overlaid. The neutral damping is smaller than the neoclassical damping in all but QHS in the symmetry direction.

the difference neoclassically. This increase is also larger than the calculated neutral damping, suggesting that there is an additional anomalous damping in the symmetry direction, which is a similar result to the tokamak flow in the toroidal direction[33]. This suggests that although neutral damping and neoclassical damping matter in the edge, there are anomalous terms that dominate the flow damping. These probe measurements measured to an  $r/a$  value of .7 and outward in .5 T plasmas, however, and therefore the conclusions drawn does not necessary translate into the core results measured in the thesis.

### 2.3.3 Turbulence driven radial electric field and flows

Turbulence can effect flows in several ways. First, the turbulence can increase the viscosity beyond the neoclassical values. This has been seen in tokamaks and in the edge of HSX[33]. Cross field viscosity can also damp the flow in the symmetry direction[35]. These effects can reduce the parallel flow and flatten the velocity profiles. By including cross field diffusion to

PENTA calculations the radial electric field was profile is flattened (and thereby the flow profile), but by including only the neoclassical level of cross field transport (see fig...) the radial electric field is still smaller than predicted in the core [15]. By adding an additional anomalous transport, presumably from turbulence, the agreement improves further. IS THIS RIGHT; SOMETHING SEEMS SLIGHTLY OFF

In addition to an increase in viscosity, in certain situations the flows in stellarators can be determined by turbulence instead of by neoclassical transport. In a tokamak and a perfectly symmetric stellarator, the flows are free flowing in the direction of symmetry and are independent of the neoclassical currents[35]. In these cases the radial current vanishes (to leading order of the gyroradius expansion) and neoclassical transport is intrinsically ambipolar. In practice it is not possible to have perfect quasisymmetry, so the question is how close does an experiment have to be to quasisymmetry to be ambipolar and how close does it need to be to have free flowing flows.

For example, in HSX, neoclassical codes predict that HSX will not be ambipolar, but will need an electric field develop to impose ambipolarity. This radial electric field would in turn impose the flows on the device. This would suggest that HSX flows are neoclassical, and not driven by turbulence. However, if the neoclassical current is small enough, the Reynolds stress and off diagonal components of the viscosity tensor can, over a given radial range, drive a radial current that can compete with or be larger than the neoclassical current[35]. The question then is, how close does a stellarator have to be to quasisymmetry and is HSX close enough. Helander and Simakov calculated the neoclassical term to dominate (assuming one is in the  $1/\nu$  regime) over a radial range  $N\rho_i$ :

$$\epsilon_{eff} = \left( \frac{L}{N\lambda_{MFP}} \right)^{\frac{2}{3}} \quad (2.7)$$

Where  $L$  is the macroscopic plasma scale length,  $N$  is the number of gyro radii in the radial region being examined, and  $\lambda_{MFP}$  is the ion mean free path. This can be rearranged into another form to find the radius at which the plasma averages to the neoclassical values of  $E_r$  [36]:

$$\Delta r_{crit} = N\rho_i = \frac{L}{\epsilon_{eff}^{\frac{3}{2}}\lambda_{MFP}}\rho_i \quad (2.8)$$

where  $\rho_i$  is the ion gyro radii and  $r_{crit}$  is the radius at which the plasma averages to the neoclassical values of  $E_r$ . These scalings have been applied to HSX. The result is that for QHS the turbulence term is larger than the neoclassical values (see figures 2.13). This suggests that the flows can be free flowing in the direction of symmetry in HSX for QHS but will be neoclassical in symmetry broken configurations.

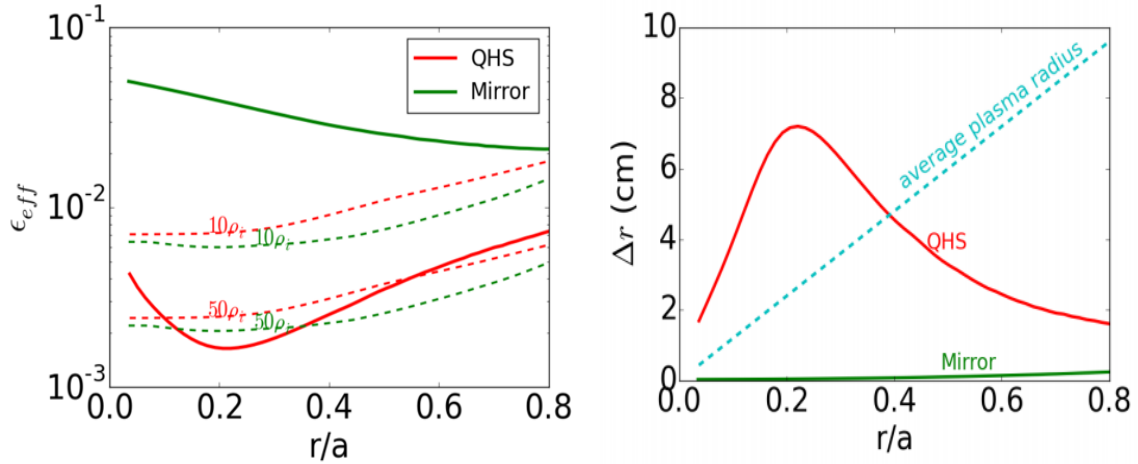


**Figure 2.13** Turbulence and neoclassical scaling. scalings.

There are a few caveats to this scaling. First, the ions are not in the  $1/\nu$  regime, this however is likely to make the scaling overestimate the neoclassical term[36]. Secondly, many details of the neoclassical and turbulence are not captured in simple scaling laws. As such a more complete comparison is needed.

In order to improve this scaling the neoclassical and Reynolds stress estimates can be replaced by calculations that can include more physics in order to find the relative importance of the various effects. The neoclassical effects will be modeled by PENTA in the following way. First, the radial current can be calculated as a function of radial electric field on each flux surface (in a normal PENTA calculation the points where the current is 0 are the solutions). If the max neoclassical radial current given by PENTA is below the value expected from Reynolds stress, then the radial electric field should be primarily set by Reynolds stress. It should be noted that the max neoclassical current calculated by PENTA is at the resonance where DKES is known to overpredict the flux and for most values of radial electric field the current is expected to be much lower than the max value.

A simple way to model the current from nonneoclassical sources here...

figure of  $E_r$  vs current and of max neoclassical flux vs

turbulence suppression and flow shear in ExB flow

## 2.4 Previous Radial Electric Field and flow Measurements on HSX

A peaked electron temperature profile and sharp temperature gradient in the core measured by Thomson scattering (see figure 1.2) and the reduction of the bootstrap current with heating power suggest the presence of the electron root in the plasma core of QHS plasmas[8]. In order to confirm this, measurements of the radial electric field have been made in a variety of plasma configurations with the CHarge EXchange Recombination Spectroscopy (CHERS) diagnostic. This is done by measuring impurity ion flows in the plasma in the toroidal and poloidal direction the radial electric field can be determined by through the force balance equation[16]:

$$E_r = \frac{1}{q_{C+6} n_{C+6}} \nabla p_{C+6} - \vec{v}_{C+6} \times \vec{B} \quad (2.9)$$

The ion pressure profile can be measured with CHERS measurements of carbon ion temperature and density. This compressive term is small in HSX due to the low ion pressure gradient. The magnetic field term is known from plasma reconstruction or field-line following and the flow is acquired from CHERS measurements of the fully stripped carbon ion flow velocity[15]. The results of these measurements showed discrepancies with the PENTA neoclassical calculations. A brief summary will be presented below (see figure 2.14), but a complete description of this work can be found in Alexis Briesemeister's paper and thesis[15, 16].

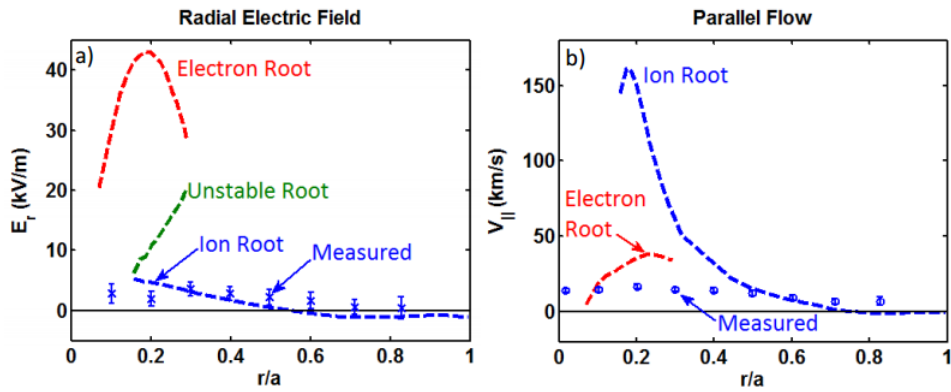


**Figure 2.14 Previous  $E_r$  & flow measurements** Measurements of the flows and  $E_r$  on methane QHS plasmas show a discrepancy with the PENTA results. The electric field is nearer to the ion root in the core, but the flow is much lower than the ion root flows. The figure is reproduced from [15].

In the previous flow measurements and radial electric field measurements, shown in figure 2.14, the measured electric field is nearer to the PENTA ion root solution and the flow that was measured was nearer to the electron root solution[15]. There are several potential reasons for this discrepancy between the measurements and the modeling results shown in figure 2.14. These include effects from the mono-energetic assumption of the PENTA code, limits arising from the previous measurements poor spatial resolution, uncertainty in the impurity density profile, the unknown level of flow induced from electron cyclotron heating and turbulence, and neutral damping. The expanded

diagnostic capabilities described in this work will reduce the impact of some of these factors on the measurement of the radial electric field.

Due to low carbon signal level, the CHERS measurement could only be made in plasmas with methane as the fill gas. The resulting high carbon content is important for several reasons, including the higher electron temperature in carbon plasmas and the change in calculated radial electric field calculated with carbon content. PENTA calculations have been found to be sensitive to the carbon density profile in methane, the measurement of which is limited. The  $C^{+6}$  charge state profile has been measured by the CHERS system, but measurements of the other carbon charge states has not been completed. Currently, the other charge states are modeled by ADAS[37] for the PENTA calculations. The uncertainty in neutral density profiles on HSX could also make the ADAS calculations inaccurate. The resulting uncertainty in impurity ion density could affect the agreement between the PENTA calculations and measurement because changing the carbon density profile changes the calculated electric field. A more complete measurement of carbon density profile is in progress, but has not yet been completed.

Another limitation of the CHERS system was that the previous poloidal views had very poor resolution in the core due to the large beam width and a collimated view. If the high electric field region was small (as expected in the PENTA calculations), the CHERS system may not have had the resolution to observe it. The need for greater resolution motivated the improvements to the CHERS measurements. The CHERS system was redesigned with focused views with 1.5 mm spot sizes instead of collimated 2.54 cm spot sizes. In addition, views were developed to measure the Pfirsch-Schlüter (PS) flow. These views look approximately in the toroidal direction and at the edges of the beam, where the radial resolution is better. This improvement in resolution should help answer the question of the existence of the electron root in the HSX plasma. Using the Pfirsch-Schlüter views, a higher radial electric field was measured than the previous CHERS



measurements, but were still below the values predicted by PENTA and were limited to methane plasmas as will be described in the rest of this work.

## 2.5 $E_r$ and Flow Evolution

It is expected that the radial electric field quickly equilibrate on HSX, on approximately the confinement timescale ( $\sim 1-2$  ms), in order to enforce the ambi-polarity constraint. However, it was unclear if the bootstrap flow and flow profile have reached their equilibrium state during the discharge, nor have measurements of radial electric field evolution been made previously on HSX. If they have not equilibrated, it could explain some of the discrepancy with the PENTA results mentioned above, because PENTA assumes that the plasma has reached its equilibrium state. The bootstrap current on HSX never reaches its steady state value in normal HSX plasmas, but estimates of the steady state values can be made by fitting the evolution in time [7]. The rate of equilibration of flow has been measured by making measurements with different beam firing times and simultaneously measuring the PS and bootstrap flows evolution throughout the discharge or by using passive measurements of flow. The flow evolution and profile will be compared to the profile evolution of the plasma current on HSX.

A scan of passive flow measurements and their evolution throughout the discharge have also been made in order to increase the time resolution of the measurements. Passive measurements lack the spatial resolution of active CHERS measurements, due to being a line integrated measurement of the whole sightline. There can be some spatial resolution due to the localization of the carbon charge states, but the resolution is still much poorer than active spectroscopy. Despite this, passive measurements are a much simpler and quicker way of doing a scan of flow with time. This is because there is only one frame of active flow measurements per shot but can get multiple passive measurements on every shot. For every active measurement, around 10 shots are averaged together to achieve the necessary signal to noise ratio and if 5 to 6 times steps are used in the scan, a very

large number of shots must be taken to achieve the desired measurement of flow evolution. This means that one scan can be made on a given runday. This makes parameter scans impractical using active flow evolution measurements. The passive measurements of the flow evolution can be made in 5-10 shots and therefore will be used, with active measurements being used to benchmark the passive flow results and to look into radial electric field evolution.

### 2.5.1 Flow and Current Evolution

The only major plasma parameter, besides ion flow velocity, that is significantly evolving in time throughout the discharge is the plasma current (the current evolves on an L/R scale which for QHS is longer than the discharge). As such, it is natural to examine if the two evolutions are linked. The link is strengthened by the fact that the flow and current are strongly related. The relation between flow and plasma current can be described by the formula  $J = e(Zn_i v_i - n_e v_e)$ . If all of the ion species are assumed to have the same velocity[15] then the equation simplifies to  $J = en_e(v_i - v_e)$ . The ion velocity can be measured with the CHERS diagnostic but the electron velocity is not measured on HSX. This means that a change, or lack of change, in the plasma current does not necessary translate to a change in ion flow. However, the electron flow can be derived from other diagnostics on HSX a rough model of the flow can be calculated using measurements from several diagnostics, including the interferometer for line averaged density, the rogowski coils for plasma current, and the passive spectroscopy system for ion flow. From these measurements a value of electron flow can be found using the following equation:

$$v_e = v_i - \frac{I_{BS}}{en_e A} \quad (2.10)$$

where A is the cross sectional area,  $I_{BS}$  is the total current, e is the electron charge,  $v_i$  is the flow measurements (an example of typical parameters and results of these calculations can be found in figure (results citation here)). This model allows for a quick calculation of electron flow

in HSX, but has some sources of error. The simple model ignores the plasma profiles, giving only a single average value for electron flow. In reality, the electron density is peaked (though stationary in time), the ion velocity profile is relatively flat, and the bootstrap current reconstructions suggest the  $J_{BS}$  profile changes significantly in time[38] (see figure 2.15). A more complete model would use a reconstruction of the plasma current as a function of time, the density profile, and the full CHERS flow evolution profile measurements. Only the simple model is compatible with the passive spectroscopy however, and therefore will be used for most of the calculations of  $v_e$  in this work, despite its limitations.

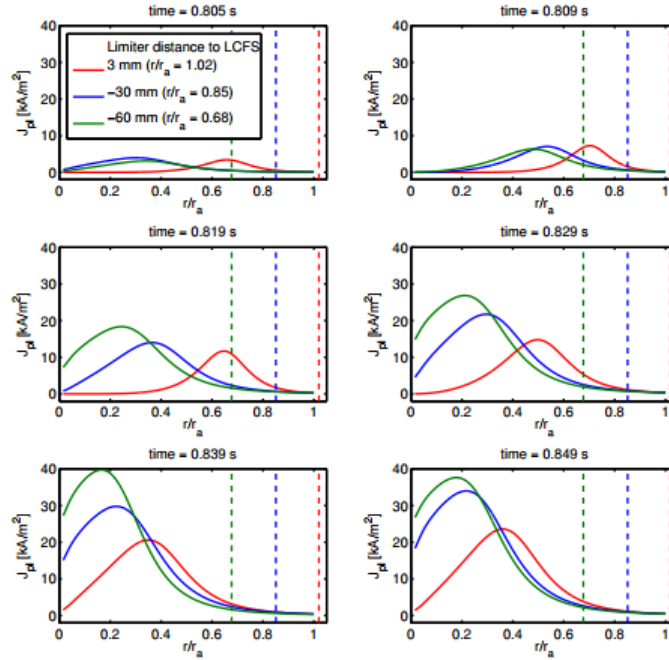


**Figure 2.15 Current profile evolution reconstruction on HSX.** The current evolution reconstruction with V3FIT was completed in QHS with three different limiter positions and 6 different time steps within the plasma. The current density becomes larger and shifts more to the core with time. The figure is reproduced from [38].

BACK EMF SECTION

The evolution of the plasma current can be described as a back EMF that opposes the rise in current that decays in time. In the beginning of the discharge, the electric field is large enough to cancel out the bootstrap current (by making the electron and ion flow velocities equal). This electric field acts on the ions and electrons in the opposite way due to their charge, but will also have a different effect due to their very disparate masses. As it decays, one would expect its effect to be more significant on the electrons than the ions ( $\frac{a_e}{a_H} = -\frac{m_H}{m_e} = -1836$ ). As such, the change in flow as the back EMF decays is expected to be primarily on the electrons. For example, a 20 km/s change in electron velocity ( $\sim$ QHS value) would lead to a .01 km/s change in ion flow. This would not explain the ion flow decay seen on HSX, because the effect is too small and in the wrong direction. The back EMF can be examined by looking at the loop voltage in the plasma (see fig).

plot of loop voltage.

**FRICTION/RESISTIVITY SECTION** Although the current evolution is expected to have a small direct effect on ion flow, it may indirectly effect the ion flow. As the current increases the friction force between the ions and electron will also increase. The friction force density is equal to:

$$F_i = m_i n_i \nu_{ie} (v_e - v_i) = -\frac{m_i \nu_{ie} J_{BS}}{e} \quad (2.11)$$

This force acts to bring the ions and electrons into the same velocity and would therefore decrease the ion flow. This would lead to a decrease in ion flow in time, which is consistent to the measurements. . Timescale of this friction.

## 2.5.2 PENTA and flow and current Evolution

PENTA gives steady state calculations of flow and  $E_r$ , but can be used to find the expected current and flow evolution with some post processing of the PENTA data. How this is done will be explained in this section.

Step 1: Run PENTA normally.

Step 2: Use PENTA to calculate the dependency of flow on  $E_{\parallel}$ . This is done by PENTA by setting the input `calc_inductive_flow` to 1. The comments say “If this flag is set, PENTA is run normally until the fluxes and flows are evaluated at the ambi-polar roots. At this point the density temperature gradients are set to zero and the quantity  $\langle BE_{\parallel} \rangle / \langle B^2 \rangle^{1/2}$  is set to 1. The flows (and fluxes) returned are then the inductive flows for a unity valued excitation.” The output gives flows as a function of  $E_{\parallel}$  ( $v_a = \alpha_a E_{\parallel}$  where  $a$  is the species in question).

Step 3: Calculate the resistivity as from the proceeding information from PENTA. The back electromotive force (EMF) that arises to oppose the bootstrap current and then decays with time can be calculated from the resistivity. The resistivity can be calculated from PENTA in the following manner:

$$E_{\parallel} = \eta J \quad (2.12)$$

$$v_a = \alpha_a E_{\parallel} \quad (2.13)$$

$$J = en_e(v_i - v_e) \quad (2.14)$$

$$J = en_e(\alpha_i - \alpha_e)E_{\parallel} \quad (2.15)$$

$$\eta = \frac{1}{en_e(\alpha_i - \alpha_e)} \quad (2.16)$$

Step 4: Use the resistivity and current to find the  $E_{\parallel}$  to balance the bootstrap current at time equals to 0.

Step 5: Find the rate of increase in total plasma current by fitting the measured current with the function:  $I(t) = I_{SS}(1 - e^{-\lambda t})$

Simple model: Scale the plasma current from PENTA to scale as  $J(r, t) = J_{SS, PENTA}(r)(1 - e^{-\lambda t})$ . This ignores the change in current rise time with resistivity, but is used as a check of the model. The change in current with time can be used to find  $E_{\parallel}$  as a function of time. When  $E_{\parallel}$  is

know, the dependency of flow on  $E$  calculated previously by PENTA can be used to find the ion and electron flow velocity with time.

A more complete model: Scale the growth of current density as a function of time with the resistivity such that  $J(r, t) = J_{SS, PENTA}(r)(1 - e^{-\lambda(r)t})$ . The value of  $\lambda$  is the resistivity at the flux surface times a constant. This constant is used to match the total plasma currents growth rate with the experimental value of total growth rate calculated previously.

## References

7. Watanabe, K. *et al.* Effect of collisionality and radial electric field on bootstrap current in the Large Helical Device. *Nuclear Fusion* **35**, 335 (1995).
8. Schmitt, J. C., Talmadge, J. N., Anderson, D. T. & Hanson, J. D. Modeling, measurement, and 3-D equilibrium reconstruction of the bootstrap current in the Helically Symmetric Experiment. *Physics of Plasmas* **21** (2014).
11. Ida, K. Experimental studies of the physical mechanism determining the radial electric field and its radial structure in a toroidal plasma. *Plasma Physics and Controlled Fusion* **40**, 1429 (1998).
12. Coronado, M. & Talmadge, J. N. Evolution of the plasma rotation and the radial electric field for a toroidal plasma in the Pfirsch-Schluter and plateau regimes subject to a biased electrode. *Physics of Fluids B: Plasma Physics* **5**, 1200–1212 (1993).
13. Spong, D. A. Generation and damping of neoclassical plasma flows in stellarators. *Physics of Plasmas* **12** (2005).
14. Lore, J. *et al.* Internal electron transport barrier due to neoclassical ambipolarity in the Helically Symmetric Experiment). *Physics of Plasmas* **17** (2010).
15. Briesemeister, A. *Measurement and Modeling of the Flows and Radial Electric Field in the HSX Stellarator* PhD thesis (UW-Madison).
16. Briesemeister, A., Zhai, K., Anderson, D. T., Anderson, F. S. B. & Talmadge, J. N. Comparison of the flows and radial electric field in the HSX stellarator to neoclassical calculations. *Plasma Physics and Controlled Fusion* **55**, 014002 (2013).

17. Maassberg, H. *et al.* Experimental and neoclassical electron heat transport in the LMFP regime for the stellarators W7A, L2, and W7AS. *Physics of Fluids B: Plasma Physics* **5**, 3627–3640 (1993).
18. Burhenn, R. *et al.* On impurity handling in high performance stellarator/heliotron plasmas. *Nuclear Fusion* **49**, 065005 (2009).
19. Maaberg, H. *et al.* The neoclassical Electron Root feature in the Wendelstein-7-AS stellarator. *Physics of Plasmas* **7**, 295–311 (2000).
20. Ida, K. *et al.* Observation of toroidal flow antiparallel to the  $E \times B$  drift direction in the hot electron mode plasmas in the compact helical system. *Physical Review Letters* **86**, 3040–3043. ISSN: 0031-9007 (Apr. 2001).
21. Sugama, H., Watanabe, T.-H., Nunami, M. & Nishimura, S. Quasisymmetric toroidal plasmas with large mean flows. *Physics of Plasmas* **18**, 082505 (2011).
22. Talmadge, J. N. & Gerhardt, S. P. Numerical calculation of the Hamada basis vectors for three-dimensional toroidal magnetic configurations. *Physics of Plasmas* **12**, 072513 (2005).
23. Gerhardt, S. P., Talmadge, J. N., Canik, J. M. & Anderson, D. T. Measurements and modeling of plasma flow damping in the Helically Symmetric eXperiment. *Physics of Plasmas* **12**, 056116 (2005).
24. Boozer, A. H. Guiding center drift equations. *The Physics of Fluids* **23**, 904–908 (1980).
25. Jaeger, E. & Jr., C. H. Radial transport in the ELMO Bumpy Torus in collisional regimes. *Nuclear Fusion* **19**, 443 (1979).
26. Beidler, C. D. *et al.* ICNTS - Impact of Incompressible ExB Flow in Estimating Mono-Energetic Transport Coefficients. *poster presented at Joint Conference of 17th International*



*Toki Conference on Physics of Flows and Turbulence in Plasmas and 16th International Stellarator/Heliotron Workshop, Ceratopia Toki, Gifu (2007).*

27. Landreman, M. The monoenergetic approximation in stellarator neoclassical calculations. *Plasma Physics and Controlled Fusion* **53**, 082003 (2011).
28. Landreman, M. & Catto, P. J. Effects of the radial electric field in a quasisymmetric stellarator. *Plasma Physics and Controlled Fusion* **53**, 015004 (2011).
29. Simakov, A. N. & Helander, P. Plasma rotation in a quasi-symmetric stellarator. *Plasma Physics and Controlled Fusion* **53**, 024005 (2011).
30. Garren, D. A. & Boozer, A. H. Existence of quasihelically symmetric stellarators. *Physics of Fluids B: Plasma Physics* **3**, 2822–2834 (1991).
31. .
32. Cornelis, J., Sporken, R., van Oost, G. & Weynants, R. Predicting the radial electric field imposed by externally driven radial currents in tokamaks. *Nuclear Fusion* **34**, 171 (1994).
33. Gerhardt, S. P., Talmadge, J. N., Canik, J. M. & Anderson, D. T. Measurements and modeling of plasma flow damping in the Helically Symmetric eXperiment. *Physics of Plasmas* **12**, 056116 (2005).
34. Gerhardt, S. P. *Measurements and Modeling of the Plasma Response to Electrode Biasing in the HSX Stellarator* PhD thesis (UW-Madison).
35. Helander, P. & Simakov, A. N. Intrinsic Ambipolarity and Rotation in Stellarators. *Phys. Rev. Lett.* **101**, 145003 (14 Sept. 2008).
36. PhD thesis ()
37. Summers, H. P. *The ADAS User Manual, version 2.6* (2004).

38. Chlechowicz, E. *IMPROVED PLASMA EQUILIBRIUM RECONSTRUCTION FOR THE HSX STELLARATOR USING AN OPTIMIZED ARRAY OF MAGNETIC COILS* PhD thesis (UW-Madison).

## Chapter 3

### Pfirsch-Schlüter CHERS Diagnostic

#### 3.1 CHERS Diagnostic Background

The CHERS diagnostic [39], and spectroscopy more generally, are used to measure the plasma velocity, temperature, and ion density in many plasma devices [cite]. These measurements can then be used to calculate the plasma's radial electric field and bootstrap flow. How this is achieved on HSX will be explained in this chapter.

HSX uses two spectrometers to measure of radiation intensity as a function of wavelength. By tuning the spectrometers to a wavelength of interest, the Doppler shift of light given off by the partially ionized ions in the plasma (fully ionized particles do not give off line radiation) can be measured. By measuring the change in wavelength from the wavelength at rest, the ion velocity can be recovered from this measurement.

The wavelengths of a specific line emission is known and for a single ion the formula for finding velocity from a Doppler shift is:  $\frac{v}{c} = \frac{\lambda - \lambda_0}{\lambda_0}$ . In a plasma however, the particles have a distribution of velocities (and temperatures), that complicates this picture. If a thermal Maxwellian distribution is assumed, then the line shape of a transition (ignoring line structure) becomes:

$$F(\lambda) = Ae^{-\frac{[\lambda - (\lambda_0 + \delta\lambda)]^2}{2\sigma_\lambda^2}} \quad (3.1)$$

Where  $\delta\lambda$  is the shift due to ion flow, A is the amplitude of the line, and  $\sigma_\lambda^2$  is the variance determined by ion temperature and instrumental broadening. The resulting formulas for the velocity and temperatures (ignoring and instrumental broadening) are:

$$v = c \frac{\delta\lambda}{\lambda_0} \quad (3.2)$$

$$kT = m_i \left( \frac{c\sigma_\lambda^2}{\lambda_0} \right)^2 \quad (3.3)$$

The density of the impurity ions can also be found because the total signal is proportional to ion density, but this was not examined in this work, so the process of making this measurement will not be explained in more detail here.

The simplest way of making this measurement is to have a fiber optic cable/s viewing the plasma connected to a spectrometer. This measurement will give the average flow of the plasma in the direction of the fiber. For the remainder of this work this method is called passive spectroscopy. The disadvantage of this method is that it gives a line integrated measurement, which makes the interpretation difficult. Another disadvantage is that in high temperature and dense fusion plasmas there most ions are fully stripped and there are few neutrals available to charge exchange with. This results in the signal being localized to the edge. In HSX however, the temperature is low enough and neutral pressure high enough that higher Z impurities can be found in the core that are not fully stripped (SEE FIGURE....). This allows measurements to be made in the core of HSX, by measuring the emission of light from line emission from a excited state to a ground (or lower energy) state. On HSX, lines of Carbon were used, specifically the 529.1 nm line emitted by  $C^{+5}$  ions when decaying from the n=8 state to n=7 state. The  $C^{+5}$  particles can get excited by collisions with the plasma, like electron impact collisions ( $C^{+5} + e^- \rightarrow C^{+5*}$ ). After getting excited they quickly decay, giving off the light measured by the spectrometers. The reasons this line was chosen was described in detail here[15], but will quickly be summarized here. The line was within the range of wavelengths detectable by the HSX spectrometers, was clear from other impurities, and was a relatively strong carbon line.

To make a localized measurement the CHERS (CHarge Exchange Recombination Spectroscopy) diagnostic is used. It works by using a neutral beam to localized the measurement location. The neutral particles charge exchange with the ions in the plasma. These particles can then emit light, which would be measured the same way as passive spectroscopy. The reaction for this is  $C^{+6} + H^0 \rightarrow C^{+5*} + H^{+1}$ . In reality the spectrometers measure both the light from the beam and the line averaged signal from the background  $C^{+5}$  mentioned before. In order to find the signal from only the beam, a suitable subtraction must be made. In HSX this is done by subtracting the signal from the frame immediately prior to the frame containing the beam.

### 3.1.1 Fitting and Calibration

In order to make the measurement of flow, two Czerny-Turner spectrometers are used to look at the carbon lines mentioned above. The following section will describe how the system is calibrated and the data fit. The fitting of the spectral lines can be seen in figure 3.1. The lines are fit by Gaussians and the central wavelength can then be found from the fitting. For CHERS measurement the previous frame is subtracted off of the beam frame to get the signal induced by the beam. This subtraction leads to a larger uncertainty and as such several shots (10-20 depending on the Carbon signal level) are averaged together to improve the statistics prior to the fitting.

In order to accurately measure the velocity a careful wavelength calibration is necessary. This calibration of wavelength of the spectrometer was calibrated in two ways. Both methods use a neon calibration lamp that has three lines in the vicinity of the Carbon line. The wavelengths of these three lines are known and can be used to find relationship between the pixel number and the wavelength distribution of the spectrometer. Fits of the three lines are used to fine the pixel to wavelength dependence of every channel. Two methods of fitting the data were compared by linearly and quadratically fitting the three data points. Both methods gave similar results, so the linear fitting was used (see figure 3.2).

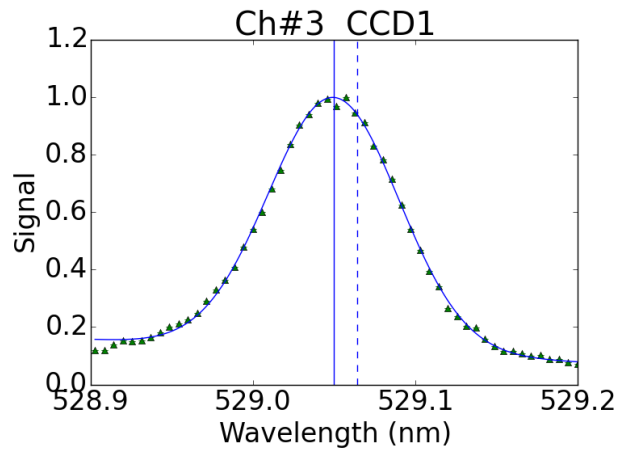


**Figure 3.1 The fit of Carbon line.** The fit and experimental data of a fit to passive spectroscopy data is plotted (note the uncertainty in the data is not plotted for clarity). The vertical lines are the center wavelength of the fit and the rest wavelength of the carbon line.

Due to the alignment of the fibers compared to the spectrometer, there tends to be a wavelength offset between channels. This is calibrated away by measuring the neon lines with all channels of the spectrometer. This allows the measurement of all of the channels dependence of wavelength. The results of this calibration can be seen in figure 3.2. After this calibration is done, it is applied to all channels as a starting point of the calibration.

The second step on the calibration is needed because the wavelength of the spectrometer can shift throughout a runday. This calibration is done by having one channel look at the Neon lines. By measuring the drift of the line every shot, the offset can be found. This offset is then applied to every channel.

### 3.2 Pfirsch-Schlüter CHERS Diagnostic Background

The old CHERS system on HSX had poor spatial resolution. This arose from two factors. First, the views had one inch collimated views and this is a significant size compared to the size of the device (see figure 3.6). Secondly, the poloidal views in the core could not resolve poloidal flows

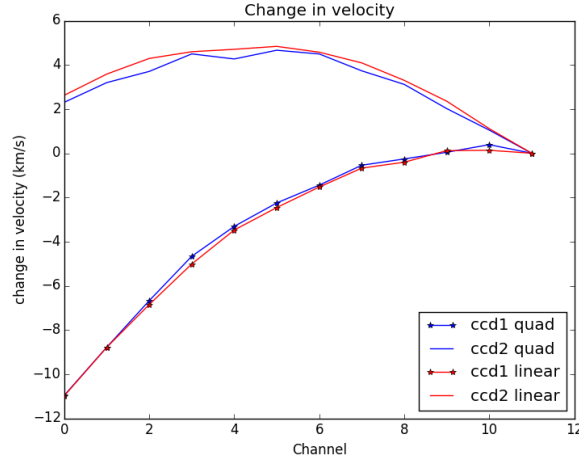


**Figure 3.2 Calibration of the spectrometer channel.** The calibration of every channel on both spectrometers was completed. Two methods of calibration were completed by linearly and quadratically fitting the three data points. Both methods gave similar results.

accurately in the core because the flux surface shape changes considerably within the view, which lead the direction of poloidal flow to drastically change direction throughout the view. As such, a new technique to calculate the flow and radial electric field has been developed that did not use the poloidal views and had focused views with 1.5mm spot size.

This method makes measurements of parallel flow at different locations on a flux surface to calculate the flow and radial electric field. The theory behind using measurements of parallel flow to find  $E_r$  and flow using a CHERS system will be laid out in this section. The general idea is that if measurements of parallel flow are made at two points on a flux surface, the radial electric field and bootstrap flows can be recovered from the difference and average flows.

The parallel flow at any point on a flux surface can be described as a flux surfaced averaged “bootstrap” flow ( $\vec{v}_{BS}$ ) and a Pfirsch-Schlüter flow ( $\vec{v}_{PS}$ ) such that  $\vec{v}_{||i} = \vec{v}_{PS} + \vec{v}_{BS}$ . The bootstrap flow is defined by  $\vec{v}_{BS} = \frac{\langle v_{||i} B \rangle}{\langle B^2 \rangle} \vec{B}$ . The Pfirsch-Schlüter flow arises due to the incompressibility of the ion flows and varies across a flux surface such that its flux surface average is zero. The

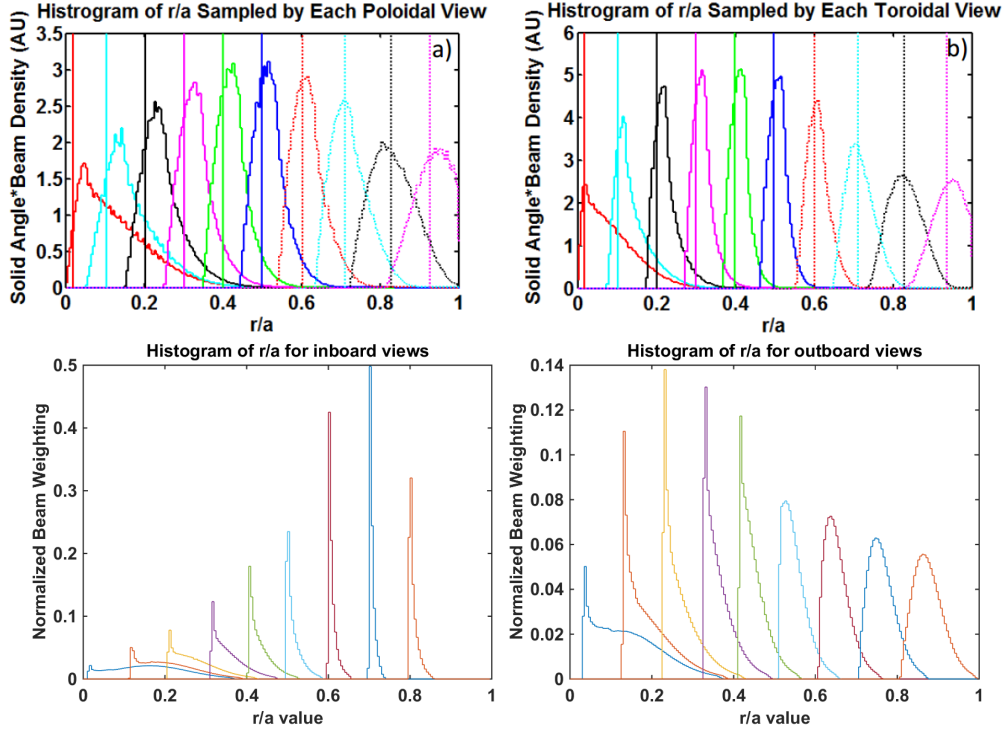


**Figure 3.3 Resolution of the CHERS views.** The resolution of the old views are compared to the new views. The new views have slightly better resolution, but the reduction improvement is limited by the cross section of the beam and views line of sight. The first figure is reproduced from [15]

incompressibility of ion flows leads to the requirement that:

$$\nabla \cdot (\vec{v}_{\parallel i} + \vec{v}_{\perp i}) = 0 \quad (3.4)$$

where  $\vec{v}_{\parallel i}$  and  $\vec{v}_{\perp i}$  are the parallel and perpendicular ion flow respectively. The perpendicular flow is proportional to the radial electric field and ion pressure gradient and can be described by:

$$\vec{v}_{\perp i} = \frac{\vec{E}_r \times \vec{B}}{B^2} - \frac{\nabla P_i \times \vec{B}}{en_i Z_i B^2} = - \left( \frac{d\phi}{d\psi} + \frac{1}{en_i Z_i} \frac{dP_i}{d\psi} \right) \left( \frac{\nabla \psi \times \vec{B}}{B^2} \right) \quad (3.5)$$

where  $\psi$  is the toroidal flux and  $\phi$  is the electric potential. Using equations 3.4, 3.5, and the definitions of the bootstrap and PS flows, the resulting Pfirsch-Schlüter flow is:



$$\vec{v}_{PS} = \left( \frac{d\phi}{d\psi} + \frac{1}{en_i Z_i} \frac{dP_i}{d\psi} \right) h \vec{B}, \quad (3.6)$$

where  $h$  is a geometric factor,  $\psi$  is the toroidal flux, and  $\phi$  is the electrostatic potential. HSX has a small ion pressure gradient, due to its cold ions, so the equation reduces to:

$$\vec{v}_{PS} = \frac{d\phi}{d\psi} h \vec{B}, \quad (3.7)$$

The geometric factor  $h$  is defined as:

$$\vec{B} \cdot \nabla h = -2 \frac{(\vec{B} \times \nabla B) \cdot \nabla \psi}{B^3} h \vec{B}, < h B^2 > = 0 \quad (3.8)$$

The CHERS system can be used to measure the total parallel flow, and if two measurements are made on the same flux surface, where  $\vec{v}_{BS}$  would be equal, and the geometric factors are known, then  $\vec{v}_{BS}$ ,  $\vec{v}_{PS}$ , and  $\frac{d\phi}{d\psi}$  can be found.  $\frac{d\phi}{d\psi}$  and  $\vec{v}_{BS}$  can then be compared to the PENTA calculation. The use of this method and the comparison to the PENTA calculations can be found in figure 4.5. More details on the diagnostic setup and experimental results can be found reference [9].

In reality, the views are not perfectly parallel to the magnetic field, but have a radial component and a small perpendicular component. It is assumed that the radial flow is  $\sim 0$  and can be ignored, but the perpendicular flow is not necessarily ignorable. The total measured ion flow will then be:

$$v_{Measured} = - \left( \frac{d\phi}{d\psi} + \frac{1}{en_i Z_i} \frac{dP_i}{d\psi} \right) \left( \hat{r} \cdot \frac{\nabla \psi \times \vec{B}}{B^2} \right) + \left( \vec{v}_{BS} + \left( \frac{d\phi}{d\psi} + \frac{1}{en_i Z_i} \frac{dP_i}{d\psi} \right) h \vec{B} \right) \cdot \hat{r} \quad (3.9)$$

[15]

The first term is the component of the perpendicular flow in the direction of the view, the second and third term are the components of the parallel flow in the direction of the view. Notice that the first and third term (the PS and perpendicular terms) are both proportional to the radial electric field, though this is multiplied by a different geometric term. The geometric factors for the three

terms (PS, bootstrap, and perpendicular flows factors) are calculated and used in this work to find.

These factors will be called  $G_{PS}$ ,  $G_{\parallel}$ , and  $G_{\perp}$  and are equal to:

$$\begin{aligned} G_{\parallel} &= \hat{r} \cdot \vec{B} \\ G_{PS} &= h \vec{B} \cdot \hat{r} \\ G_{\perp} &= -\hat{r} \cdot \frac{\nabla \psi x \vec{B}}{B^2} \end{aligned} \tag{3.10}$$

Both the perpendicular flow and the PS flow are proportional to  $E_r$  (see equation 3.10), so the  $G_{PS}$ ,  $G_{\perp}$  terms can be added together to get  $G_{\perp+PS} = -\hat{r} \cdot \frac{\nabla \psi x \vec{B}}{B^2} + \hat{r} \cdot \vec{B}$ . These can then be used to find the flow and  $E_r$  by solving the following matrix:

$$\begin{bmatrix} G_{\parallel \text{ inboard}} & G_{(\perp+PS) \text{ inboard}} \\ G_{\parallel \text{ outboard}} & G_{(\perp+PS) \text{ outboard}} \end{bmatrix} \begin{bmatrix} v_{BS} \\ \frac{d\phi}{d\psi} + \frac{1}{en_i Z_i} \frac{dP_i}{d\psi} \end{bmatrix} = \begin{bmatrix} V_{\text{Measured inboard}} \\ V_{\text{Measured outboard}} \end{bmatrix}$$

The geometric factor for the PS views are shown in figure 3.4. The large difference in the PS factor between the inboard and outboard side allows for the measurement of radial electric field. Although the views were designed to be parallel views, the perpendicular geometric factor is nonzero. In the core the perpendicular term is small, but it grows larger near the edge. However, there is a relatively small difference in between the inboard and outboard side views. This means that the term is more important for the calculation of the bootstrap flow than the radial electric field. When calculations are made of  $E_r$  and bootstrap flow, with and without the perpendicular component, the change in radial electric field calculated is small, typically much smaller than the measurement error. The change in bootstrap flow is small in the core, but becomes comparable or even larger than the measurement uncertainty. Due to the non-negligible effect of the perpendicular component, all the terms were used in the following analysis.

This method of using all of the geometric factors is also a general solution, and can be applied to any two views looking at a flux surface (for example, the old CHERS views). Two other complications arise from the fact that the two views sample a volume containing many flux surfaces,

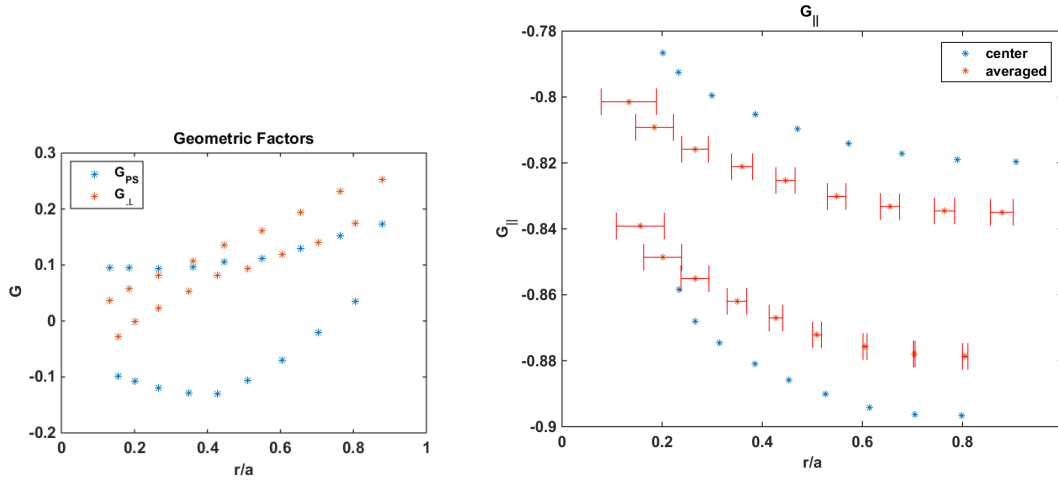


**Figure 3.4 The CHERS Geometric Factors of the Pfirsch-Schlüter views** The left plot includes the PS geometric term and compares it to the perpendicular term geometric term. In the core the perpendicular term is small, but it grows larger near the edge. There is a relatively small difference in between the inboard and outboard side however. The parallel geometric factors at the focal point and the sightline averaged values are plotted in the second figure. There is a relatively small difference in this term across the views.

not just a single flux surface. This lead to the development of a synthetic diagnostic to take all of this into account. The synthetic diagnostic will be described in the next section. The second complication is that the two views that are designed to look at the same flux surface do not actually do so. This is due to the as built views being slightly different than they were designed and, in some configurations, there is an axis shift that that leads the beam to not be centered on the magnetic axis. In non axis shifted configurations this effect is small, but in configurations that have a shifted axis the asymmetry of the inboard and outboard viewing positions is larger. In order to calculate the bootstrap flow and radial electric field from views not on the exact same flux surface, the values of net flow and the geometric quantities of interest from the outboard channels are interpolated in  $r/a$  space to match the  $r/a$  values of the inboard channels (see figure 3.4).

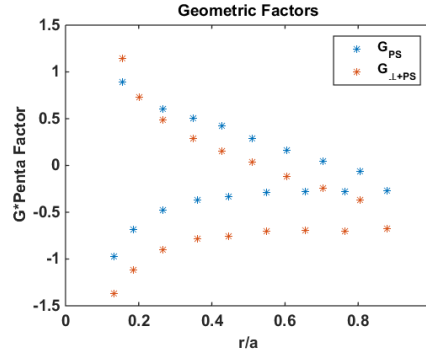


**Figure 3.5 The CHERS Geometric Factors of the Pfirsch-Schlüter views** The left plot includes the PS geometric term and compares it to the combined PS and perpendicular terms. The geometric factors are multiplied by the PENTA conversion factor, which is peaked in the core. The parallel geometric factors at the focal point and the sightline averaged values are plotted in the second figure. There is a relatively small difference in this term across the views.

### 3.3 The Neutral Beam Synthetic Diagnostic

In order to compare neoclassical calculations, like those done with the PENTA code, with experimental results from the CHERS system a synthetic diagnostic was developed. The details of this synthetic diagnostic are laid out in this section. First, the PENTA model and diagnostic neutral beam will be briefly described, then the details of the synthetic diagnostic will be laid out.

#### 3.3.1 PENTA Neoclassical Modeling

The neoclassical calculations in this work used the PENTA code[13, 14]. PENTA uses the DKES code to calculate solutions to the linearized drift kinetic equation (DKE). PENTA uses coefficients from DKES to calculate the flux of ions and electrons as a function of  $E_r$  in combination with terms that include momentum correction. The radial electric fields that give equal electron and ion fluxes are found. This is necessary to maintain quasi-neutrality in the plasma. There can be several different values of  $E_r$  where the fluxes are matched however, called roots, in the HSX plasmas. Typically there are three different types of roots, electron roots, with high electric fields and lower fluxes, ion roots with lower electric fields (and typically negative  $E_r$  if  $T_i \sim T_e$ ), and

unstable roots. Outside the mid-radius only ion root solutions are calculated to exist. Inside the core, a region where all the roots exist occurs in most plasmas on HSX. In the highest temperature plasmas of HSX there can be electron root only solutions in the core as well. Besides the flux and radial electric fields used to find a given root, PENTA gives the expected parallel flow and bootstrap current levels as outputs on a flux surface.

The radial electric field is not necessarily constant on a flux surface nor across flux surfaces. As such, the measured electric field may not (and very likely will not) be the same as the flux surface averaged value at the point of measurement. Therefore, using a non-flux surfaced averaged electric field profile is necessary to model the expected electric field that will be measured by the diagnostic system. PENTA outputs the flux function  $E_{r_{PENTA}} = -d\phi/dr_{PENTA}$  which can be used to find the local electric field. The equations for converting the PENTA fields to local fields are [15, 16]:

$$r_{PENTA} = \sqrt{\frac{\psi}{\pi B_o}} \quad (3.11)$$

$$E_{r_{PENTA}} = -\frac{d\phi}{dr_{PENTA}} \quad (3.12)$$

$$-\frac{dr_{PENTA}}{d\psi} = \frac{1}{2} \sqrt{\frac{1}{\psi \pi B_o}} \quad (3.13)$$

$$-\frac{d\phi}{d\psi} = \frac{1}{2} \sqrt{\frac{1}{\psi \pi B_o}} E_{r_{PENTA}} \quad (3.14)$$

$$E_{r_{local}} = -\frac{d\phi}{dr} = -\frac{d\phi}{d\psi} \frac{d\psi}{dr} = \frac{1}{2} \sqrt{\frac{1}{\psi \pi B_o}} E_{r_{PENTA}} \frac{d\psi}{dr} \quad (3.15)$$

Where  $\phi$  is the electric potential and  $\psi$  is the toroidal flux. These equations were implemented into the synthetic diagnostic to calculate the local electric field at points within the sightline volume from a given PENTA calculation of a HSX plasma.

### 3.3.2 The Diagnostic Neutral Beam

The neutral beam on HSX is a 28 kV, 4 A hydrogen beam with a pulse length of 4 ms[40]. An Ocean Optics spectrometer is used to measure the energy components of the beam. The first energy component is measured to be (85-90%) of the total beam current. The beam is not measured to be perturbative to the plasma, the gas puffing remains unchanged during the beam, as do the temperature and density measured by the Thompson scattering system[15].

After being neutralized the beam passes through an aperture that reduces the beam current by 45%. In addition, Faraday cup measurements have shown that 10% of the beam is attenuated in the plasma. The remaining beam current enters the HSX vacuum vessel and is focused at slightly above the plasma core[15, 40], which is the location of the MSE and CHERS measurements. Measurements indicated that the neutralization fraction had decreased from the beams optimal value. Due to this measurement, a calorimeter was built to better diagnose the beam and to be used to optimize the beam, both in alignment and improving the neutralization fraction. More details on this work can be found in the appendix.

### 3.3.3 Neutral Beam Model

Although it is simplest to approximate the beam induced emission as originating from a single point, in reality, the light is from a volume set by the cross section of the beam and the spot size of the view. In HSX, due to a relatively small size of the plasma, as compared to the finite beam width, the sightline cuts through a significant volume of the plasma. The emission from this volume can be simulated to compare predictions from a neoclassical model like PENTA of flow and radial electric field to experimental measurements[13, 14]. Proper weighted averaging must be employed to accurately interpret the experimental measurements and compare them with theoretical calculations. To account for these effects, a synthetic diagnostic was developed to find the effect of the finite beam width and spot size on the measurement of electric field and flows to

properly compare the measurement to neoclassical calculations. The model has been applied to the optimization of the MSE polarimetry system and to the interpretation of Pfirsch-Schlüter flow measurements, though only the second is described in this work.

This modeling is important for several reasons. First, depending on the magnetic geometry and plasma parameters, the quantities of interest can significantly change within the sampling volume. For example, the sightline volume samples different values of the radial electric field and flow, both in magnitude and direction. This can lead to a measured electric field which is different from the value at the focal point of the optics. Another effect is that there is a change in the direction of the magnetic field vectors across the sightline, especially in poloidal views near the core. This leads the measured poloidal flow to vary significantly in magnitude relative to

The beam model was made by a discretization of the cross section of the sightline and beam into a grid (typically 0.1mm by 0.1mm by 0.1mm in these calculations). The flux surface averaged radial electric field and impurity ion flow are calculated using the neoclassical transport code PENTA and the magnetic field vectors, taken from VMEC, are mapped onto the 3D grid. At each point a the amount of signal expected from each volume was found in order to properly take the weighted average of the signals. The weighting was found by taking the beam profile, sightline optics (including spot size, limits on the acceptance angle due to the fiber numerical aperture, solid angle effects), emission cross sections, and experimental plasma parameters into account at each grid point. This weighting was then used to find both the average value of quantities of interest and their spread for a given view.

To properly model the etendue of the optics, at each point of the discretization the following steps were taken. Firstly, the solid angle of the light captured by the front optics was calculated. Secondly, the fraction of that light that, after passing through the optic system, would strike the fiber area, and do so at within the acceptance angle, was calculated at each point. This captures

the fact the effective spot size of the optics is not constant across the viewing volume for a focused view.

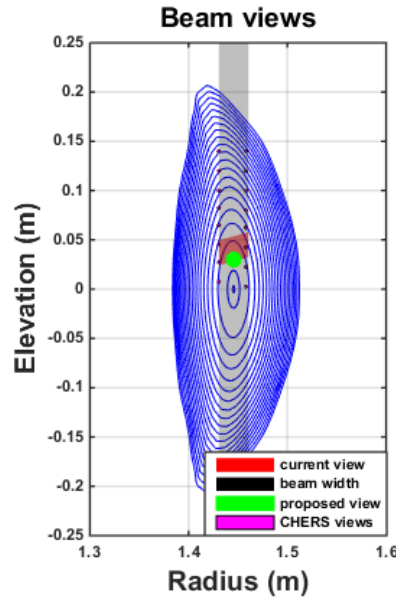


**Figure 3.6 Poloidal cross section of the HSX magnetic flux surfaces and the beam.** The gray shaded region represents the  $1/e$  width of the DNB. The existing and proposed MSE views are shown. The existing ‘poloidal’ view cuts through more flux surfaces and therefore has a larger spread in pitch angle. The proposed view is also plotted, and due to its ‘toroidal’ view it samples a smaller cross section of the flux surface and has better spatial resolution. The PS views are also plotted, but have much smaller spot sizes.

The poloidal views radial resolution is primarily limited by the beam width until the spot size diameter are near the beam width. This allows for a larger fiber with a correspondingly larger spot size to be used without sacrificing resolution in order to collect more light. The resolution for all poloidal views is poor compared to the toroidal view, as seen in figure 3.7. The toroidal views have better spatial resolution than the poloidal views above because as they pass through the beam they stay on approximately the same flux surface (the views have some radial component) as can be seen in figure 3.3.



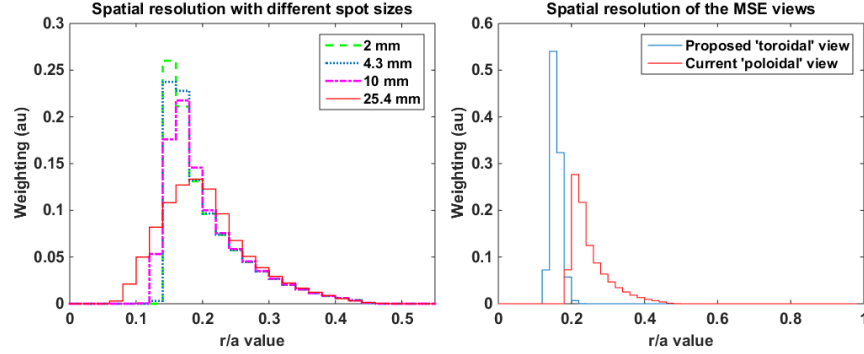


**Figure 3.7 Histogram of  $H_\alpha$  signal vs  $r/a$  for different optical spot sizes and views.** The radial resolution of the poloidal view is plotted with various spot size. The beam width creates a significant amount of signal from the outer parts of the plasma. The toroidal views have better spatial resolution than the poloidal views above because they sample fewer flux surfaces as can be seen in figure 3.3.

### 3.3.4 Atomic Physics

In order to properly model the signal strength as a function of location, atomic physics effects and plasma profile information is needed. First a description of the emission of charge exchange light throughout the sightline will be presented. Then a description of the Carbon density profile will be described. Lastly, some other atomic physics considerations will be discussed. In order to clarify some effects, the atomic physics of the CHERS system will be compared to the effects from a BES/MSE system.

The intensity of the carbon line used in HSX's CHERS system can be calculated by the following equation taken from [41, 42]:

$$S = \int dr \left( \sum_{k=1}^3 J_k(r) n_{C^{+6}}(r) \sigma_i^{C^{+6}} + n_{C^{+6}}(r) n_{H^0}(r) \langle \sigma_i^{C^{+6}}(v) v \rangle + n_{C^{+5}} \sum_{G=1}^N n_G \sigma_i^{C_G^{+5}} \right) h\nu \epsilon S \frac{\Delta\Omega}{4\pi} \quad (3.16)$$

Where  $S$  is the total emission in watts and the integration is done over the line of sight. The first term describes the charge exchange rate from the beam particles from the first three components of the beam and is proportional to the beam density,  $C^{+6}$  density, and the cross sections for

charge exchange. The second term is the charge exchange rate with neutral hydrogen (from the background neutrals or the beam plume described later). The final term of the equation arises from the excitations of the  $C^{+5}$  ions in the plasma. This can arise from multiple types of collisions (for example collisions with electrons) and is will be proportional to the  $C^{+5}$  density and the cross section and density of the exciting particle (called G). The first term is the desired measurement and the other two terms are the reason that background subtraction is necessary. When background subtraction is done only the first term will remain to first order. The beam can perturb the plasma or the neutral density, however, which can complicate the analysis. On HSX no change has been seen to the Thompson profile due to the beam firing so the effect on the plasma is thought to be small[15].

The remaining terms relate mainly to optics used to collect the light. Where  $h\nu$  is the energy of the photons,  $\epsilon$  is a scaling term that includes effects of the detector efficiencies, the fraction of light that decays from  $n=7$  to 6 instead of other pathways, and is the optical transmission efficiency. It is necessary to know for absolute density measurements, but for this work the relative signal levels is all that is required.  $dl$  is the sightline element,  $S$  is observation area along the sightline, and  $\frac{\Delta\Omega}{4\pi}$  is the fraction of the beam emission solid angle that is measured at the beam emission point. For the purpose of modeling the beam signal, this model assumes several things, including the fact that the beam is not attenuated in the viewing volume and the beam is mono-energetic. The mono-energetic condition can be relaxed by integrating over the beam distribution, but this was not done in this analysis due to the low beam temperature (a few eV) as compared to the 30 keV beam energy which makes the change in the excitation cross sections and beam velocity small. As the beam attenuation from the whole plasma is 10%, the change in beam density is very small over the spot size volume (a 1 cm diameter spot size is around 2.5% of the beam length in the plasma) making the approximation valid [15].

In order to calculate the localization of the signal and to input the correct inputs into models like PENTA the Carbon density profile is required. Measurements have been made in the past of the  $C^{+6}$  density profile and preliminary measurements of the  $C^{+5}$  density profile have been made. However, for PENTA calculations all of the charge states of carbon are required for an accurate calculation. This is necessary because in a plasma fueled with methane the carbon content of the plasma is expected to be high (around 1 Carbon for every 4 Hydrogen). Calculations of the charge states as a function of radii have therefore been made using ADAS [43]. The results can be seen in figures ???. The Carbon ions would be fully stripped in the core due to the plasma temperature, except that the high neutral density leads to charge exchange and thereby a large reduction in the fully stripped carbon in the core.

It should be noted that the ADAS calculation does not include transport across flux surfaces, and thereby will overestimate the localization of the Carbon charge states. Measurements indicate a broader  $C^{+6}$  density profile than the ADAS calculation, for example, that reaches all the way to the edge and tracks the electron density more in the edge than the ADAS calculation. As such, the electron density profile (scaled appropriately) was used in the beam model for the fully stripped Carbon density. In the core, where this work is primarily focused, the profiles should be less effected and should thereby be useful as inputs to PENTA.

Another effect seen to have an effect on the CHERS measurements in other machines is from the ‘plume’ created by the neutral beam [44]. The charge exchanged carbon can get re-excited and readmit light after the original decay before it ionizes to become a fully stripped carbon atom. The secondary emission can originate in a different position compared (for example, outside the beam volume). If this light is captured by the optics, it can lead to an incorrect measurement of flow, density, and temperature due to mis-attributing the measurement location (and thereby the geometric factors and flux surface location of the measurement). This light cannot be subtracted off from the background using the frame before because it is a beam dependent effect. What remains

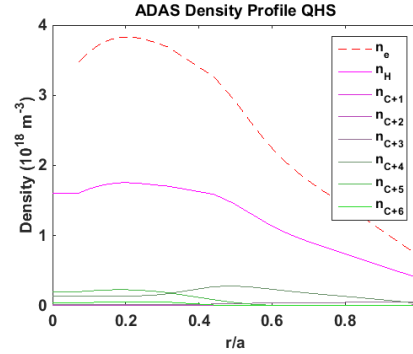


**Figure 3.8** The plasma density of each species from ADAS. The density of the ion species is calculated by the ADAS code. The Carbon ions are a significant percentage of the ion population and are therefore included in the PENTA calculation.

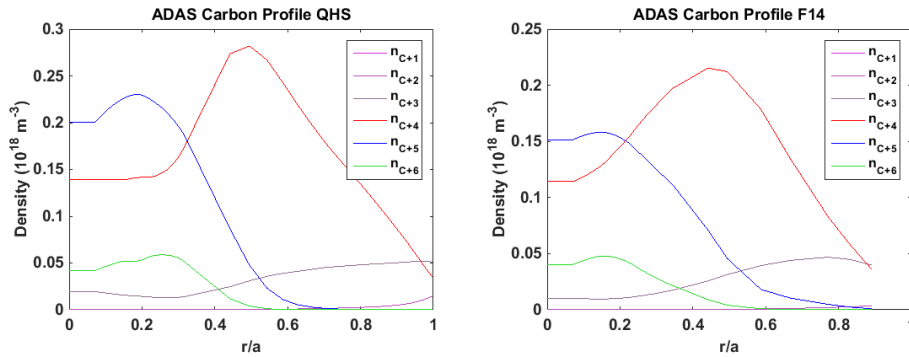


**Figure 3.9** The Carbon density calculated by from ADAS. The carbon species are calculated for QHS and F14. There is more fully stripped carbon in the QHS case than the F14 case due to the higher electron temperature in the core. All of the carbon ions are not fully stripped in the core due to the high neutral population in the core charge exchanging with the carbon ions. Note the absolute densities are different due to differences in the total plasma densities between the two cases.

then is to show the expected magnitude of these effects on HSX. One major difference between HSX and devices like NSTX is that HSX has a significant neutral population and a non-fully stripped carbon population in the core. ADAS[43] has been used to estimate the carbon species profiles and some preliminary measurements have been made of the carbon density profiles for several species. ADAS suggests that the  $C^{+6}$  has a density around  $.6 \times 10^{17}/m^3$  while  $C^{+5}$  has a density around  $2.4 \times 10^{17}/m^3$  in the core of a methane fueled plasma. If all of the  $C^{+6}$  in the

plasma became  $C^{+5}$  there would be an increase of 27% in the  $C^{+5}$  density. If you assume all of the beam neutrals charge exchange with carbon there would only be a .2% change in the  $C^{+6}$  profile (the beam attenuation is actually  $\sim 10\%$ ). This would suggest that the beam will not significantly change the background carbon profile in HSX. In addition, despite the 3.7 times higher density and larger emitting volume within the sightline the carbon signal in the non-beam frames are comparable to the active signal. This suggests that the rate of re-excitation of the  $C^{+5}$  frames is low, and that the tiny increase in  $C^{+5}$  from the beam is unlikely to have any effect.

### 3.3.5 Pfirsch-Schlüter Flow Synthetic Diagnostic

add part about including perp effects and matrix to find  $E_r$  and flow mentioned earlier???

The PS views look at the edges of the beam, but despite this, the beam width effect is not negligible and the synthetic diagnostic was used to compare the data to the models. For the Pfirsch-Schlüter views the quantities of interest are the electric potential and the geometric factors needed to calculate the Pfirsch-Schlüter effect (hB). To look at the inboard and outboard side of the plasma, the views look toroidally and at the edges of the beam. This leads to a smaller signal than from a view at the core of the beam, but it is more localized due to effectively viewing less of the beam width. Despite the better spatial resolution, the PS factors and  $E_r$  at the focal point of the optics are significantly different than their values averaged over the sightline (figure 3.10). This arises for two reasons, firstly, the views are not perfectly toroidal (the radial component is largest in the core views); this leads to sampling across flux surfaces with different values of  $E_r$ . The second effect arises from the steep gradient in beam density and, to a lesser extent, plasma density within the view. This effectively shifts the viewing location towards the center of the beam and into a region with different electric field and PS factors. This effect is more important in the core than in the edge views due to the fact that the change in  $E_r$  and PS factors due to the shift towards the center of the beam has a greater effect in the core due to its small size and the shape of the flux surfaces

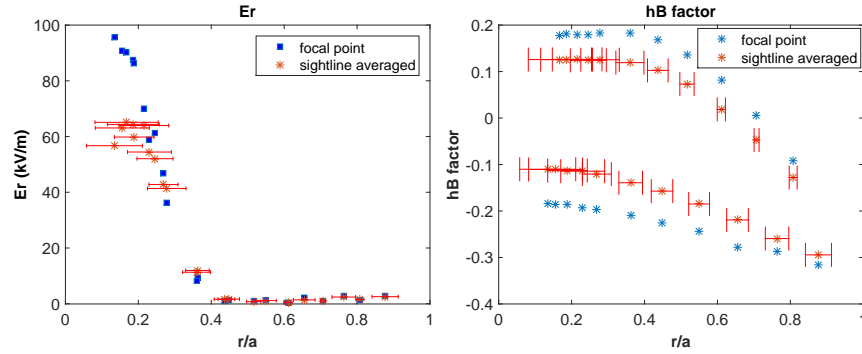


**Figure 3.10 Synthetic diagnostic of the Pfirsch-Schlüter views** Both the  $E_r$  and hB factors at calculated for the focal point of the optics are higher than the sightline averaged values in the core. This arises because in the core the focal points sample the high electric field region of a flux surface, but the size of that region is small compared to the sightline volume. The non-monotonic  $E_r$  is due to the fact that the local value of  $E_r$  changes depending on the location of measurement on a flux surface. In the edge, the gradient in  $E_r$  is small, such the larger sampling volume has little effect. The radial spread of the view is plotted for the sightline averaged views.

near the core. In addition, the model shows that although the focal points were designed to fall on the same flux surfaces, the sight-lined averaged views are offset. This offset complicates the analysis of the PS measurements.

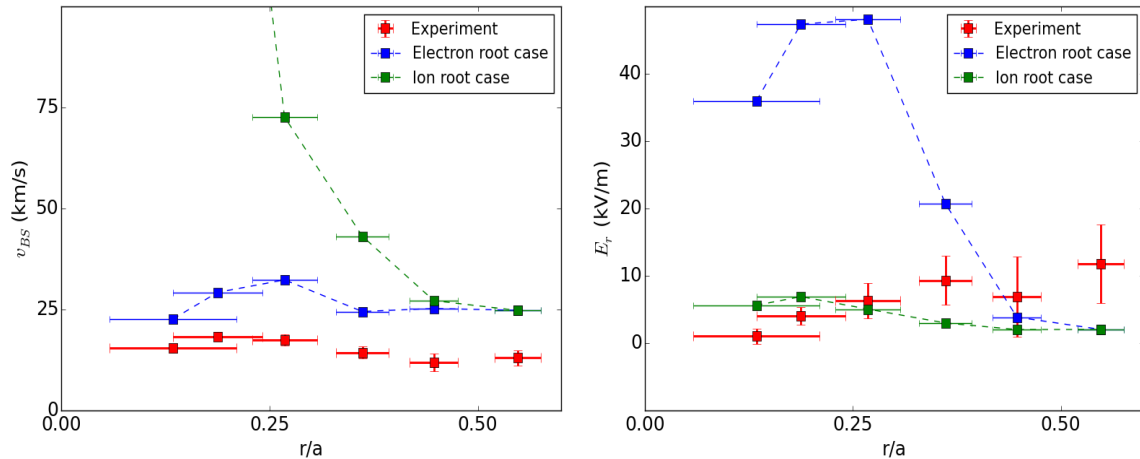


**Figure 3.11 Pfirsch-Schlüter measurement of flow and  $E_r$**  The Pfirsch-Schlüter system was used to measure bootstrap flow and  $E_r$  and the results were compared to the synthetic diagnostic values predicted if the ion or electron root from PENTA calculations were present.

### 3.4 Conclusion

The beam synthetic diagnostic is important if the quantities of interest change within the sampling volume. This is the case on HSX where changes (up to 50%) are seen between the sightline averaged signals and the signal modeled from only the focal point[10]. This was seen in calculations of flow and  $E_r$  for HSX plasmas performed for both the MSE and PS systems. Reducing the beam diameter or looking even more at the edge of the beam can reduce this effect, but in HSX these options are not viable. Therefore, properly modeling the beam is necessary to analyze the results from beam emission diagnostics on HSX. More details on how this model was applied to the MSE system and the PS system and the results of the modeling will be presented in each of their respective chapters. Additional description of the model can be found in reference [10].

## References

9. Kumar, S. T. A. *et al.* Determination of radial electric field from Pfirsch-Schluter flows in the HSX stellarator. *Nuclear Fusion* (accepted 2016).
10. Dobbins, T. J., Kumar, S. T. A. & Anderson, D. T. A synthetic diagnostic for beam emission spectroscopy in the helically symmetric experiment stellarator. *Review of Scientific Instruments* **87** (2016).
13. Spong, D. A. Generation and damping of neoclassical plasma flows in stellaratorsa). *Physics of Plasmas* **12** (2005).
14. Lore, J. *et al.* Internal electron transport barrier due to neoclassical ambipolarity in the Helically Symmetric Experiment). *Physics of Plasmas* **17** (2010).
15. Briesemeister, A. *Measurement and Modeling of the Flows and Radial Electric Field in the HSX Stellarator* PhD thesis (UW-Madison).
16. Briesemeister, A, Zhai, K, Anderson, D. T., Anderson, F. S. B. & Talmadge, J. N. Comparison of the flows and radial electric field in the HSX stellarator to neoclassical calculations. *Plasma Physics and Controlled Fusion* **55**, 014002 (2013).
39. Fonck, R. J. Charge exchange recombination spectroscopy as a plasma diagnostic tool (invited). *Review of Scientific Instruments* **56** (1985).
40. Abdrashitov, G. F. *et al.* A diagnostic neutral beam system for the MST reversed-field pinch. *Review of Scientific Instruments* **72** (2001).
41. Isler, R. C. A Review of Charge-Exchange Spectroscopy and Applications to Fusion Plasmas. *Physica Scripta* **35**, 650 (1987).
42. Kobayashi, S. Plans for intallation of Beam Emission Spectroscopy on HSX. *HSX Group meeting talk* (2015).



43. Summers, H. P. *The ADAS User Manual* ().
44. Bell, R. E. Carbon ion plume emission produced by charge exchange with neutral beams on National Spherical Torus Experiment. *Review of Scientific Instruments* **77**, 10E902 (2006).

## Chapter 4

### Measurements

#### 4.1 $E_r$ and Flow Evolution measurements

The flow in QHS plasmas are measured to evolve in time. This was seen in passive spectroscopy measurements and active CHERS measurements. This section will describe the results of the measurements of flow evolution in a variety of plasma configurations and plasma parameters. It was found that the plasma flow was evolving in only QHS configurations. These results will be presented and potential explanations for this effect will be examined.

The line averaged density in QHS was scanned in order to find the dependence of flow and flow evolution on density. The difficulty with this comparison is that changing the density changes many other plasma parameters, including the temperature and current evolution (see figure 4.1). The result is that the plasma flow is found to decrease with an increasing density (see figure 4.1), though both plasmas show deceleration. There are several explanations for this result, including the increase in power deposition per particle. Overall, the passive measurements showed a 2-4 km/s difference in flows between the two densities.

The plasma flow in both cases are found to decrease in time. The plasma current is the only plasma parameter that is evolving on this timescale. The plasma current is proportional to the flow differential between the electrons and ions.

$$J_{BS} = en(v_i - v_e) \quad (4.1)$$

A simple model to calculate what the change in differential flow resulting from a change in plasma current can be found by using the line averaged density, total plasma current and average cross sectional area of the device. The results of this model can be seen in figure 4.1. Since the CHERS measurements indicate that the flow is fairly flat across the device for most plasmas this model is not expected to be too unrealistic. A more complete model would use the active flow measurements of flow coupled with the Thompson density profile, and a plasma current reconstruction. The model suggests the flow differential in QHS would lead to a flow differential of up to 15 km/s.

In HSX the ion flow is in the direction of current and the flow is expected to significantly contribute to the plasma current [cite Schmitt paper]. Intuitively, an increasing current would lead to an increase in ion flow because a decreasing ion flow would result in the ion contribution to current decreasing in time. This is not the case however. This would suggest that the change in electron flow would have to be larger than the decrease in ion flow for this situation to occur. As such, and increasing current is a result of an increasing electron flow.

The remaining question is why the ion flow would be decreasing with time. One potential solution is that the drag between the electron and ions is increasing as the electrons speed up, which slows the electrons. The friction force between ions and electrons is:

$$F_i = m_i n_i \nu_{ie} (v_e - v_i) = -\frac{m_i \nu_{ie}}{e} J \quad (4.2)$$

This would suggest that the current increase would lead to a drag on the ions slowing them down.

Other sources of drag here.

In order to further study this problem, active CHERS measurements have been made by scanning the beam fire time throughout the discharge. This was done in 50 kW QHS plasmas (the plasma parameters and passive flow data can be seen in figure 4.3). The results of the measurements and comparison to PENTA can be seen in figure 4.2.

### 4.1.1 configuration comparisons

The active measurements of flow is below the prediction of PENTA and decreasing in time, but the flow is closer to the electron root solution. The radial electric field was measured to be close to the ion root value. In the core, where the electron root is the only root calculated to exist, no large radial electric field is measured. This result is qualitatively similar to previous measurements (cite Alexis paper/thesis and Santhosh's paper). Although the flow is measured to be evolving in time, the radial electric field is not evolving in time (within the error bar of the measurements). This would suggest that the perpendicular flow has reached equilibrium but that the parallel flow has not yet done so.

### 4.1.2 configuration comparisons

In order to examine the influence of neoclassical effects on the flow evolution other configurations with broken symmetry were examined. These configurations should have larger NC flow dampening, and have been measured to have higher flow dampening in the core (cite paper). Two auxiliary configurations were examined in this work, Old Mirror and flip 14 (F14). Old Mirror has larger symmetry breaking than the other configurations. It also has an axis shift, that makes the comparisons of flow more difficult because the same views do not measure the same area of the plasma, making comparisons of flow magnitude difficult. The results of 50 kW OM and QHS comparison are shown in figure 4.3

The flows in old mirror reach steady state on the same timescale as the current evolution and the density roll over. This agrees with the theory that the flow evolution seen on QHS is related to current evolution. The QHS has the same general behavior as the 100 kW data shown above in figure 4.1.

Comparisons were made with F14, which does not have an axis shift and therefore can more readily be compared to QHS. Active measurements from this runday were first presented here

[Santhosh paper], but will be discussed again in a later section [reference where]. The passive measurements show two interesting things. First, that only flow in QHS is evolving in time and, second, that F14 has higher flow than QHS (see figure 4.4). The current is evolving in time in F14, but the magnitude is significantly smaller than in QHS. The expected growth in flow differential between the ions and electrons during the measurement time of the flow measurement is around 3 km/s. If one assumed half of that comes from electrons and half from ions speeding up, the resulting 1.5 km/s acceleration would fall within the uncertainty of the measurement. The same cannot be said for the QHS data where the current (and therefore flow differential) is much higher.

The flow measured in active and passive spectroscopy has shown that the flow in F14 is higher than QHS. This is despite the higher calculated neoclassical dampening and measured dampening in the edge in this configuration [cite Stephan paper].

### **4.1.3 Heating power and location scan**

## **4.2 Pfirsch-Schlüter Flow Measurements**

The first results from the Pfirsch-Schlüter system show a discrepancy both in the flow and the radial electric field predicted by PENTA. The flow measurement is lower than what is predicted for either root, but were closer to the electron root values of flow. In the core, the electric field better matches the ion root. In the edge, the measured field is higher than the calculation. This can be seen in fig 4.5. This answer is qualitatively similar to the previous results (see figure []). The discrepancy between the measurements and the PENTA model may be explained by the change in plasma conditions between the times of the two measurements. The walls are now boronized, but the old measurements were made with carbonized walls, which changes the amount of impurities in the plasma.

#### **4.2.1 configuration scan**

#### **4.2.2 Heating power and location scan**

#### **4.2.3 Flow vs $E_r$ comparisons with PENTA**

The flow and radial electric field measurements do not match the PENTA predicted values for many of the measurements shown above. Another question to investigate is if the PENTA calculated dependency of  $E_r$  and parallel flow is correct. If the radial electric field is different than PENTA predicts because of effects arising from ECRH flux, charge exchange, or other effects previously mentioned that are not included in the PENTA code, the dependency of  $E_r$  and parallel flow from PENTA would not necessarily be incorrect. In order to examine this the experimentally measured values of flow and radial electric field are compared to the dependency calculated by PENTA.

### **4.3 Conclusion**

The flow of the plasma is influenced by several factors, including configuration, heating, current, and density. The difficulty when analyzing what is going on is that many of these factors are codependent on each other.

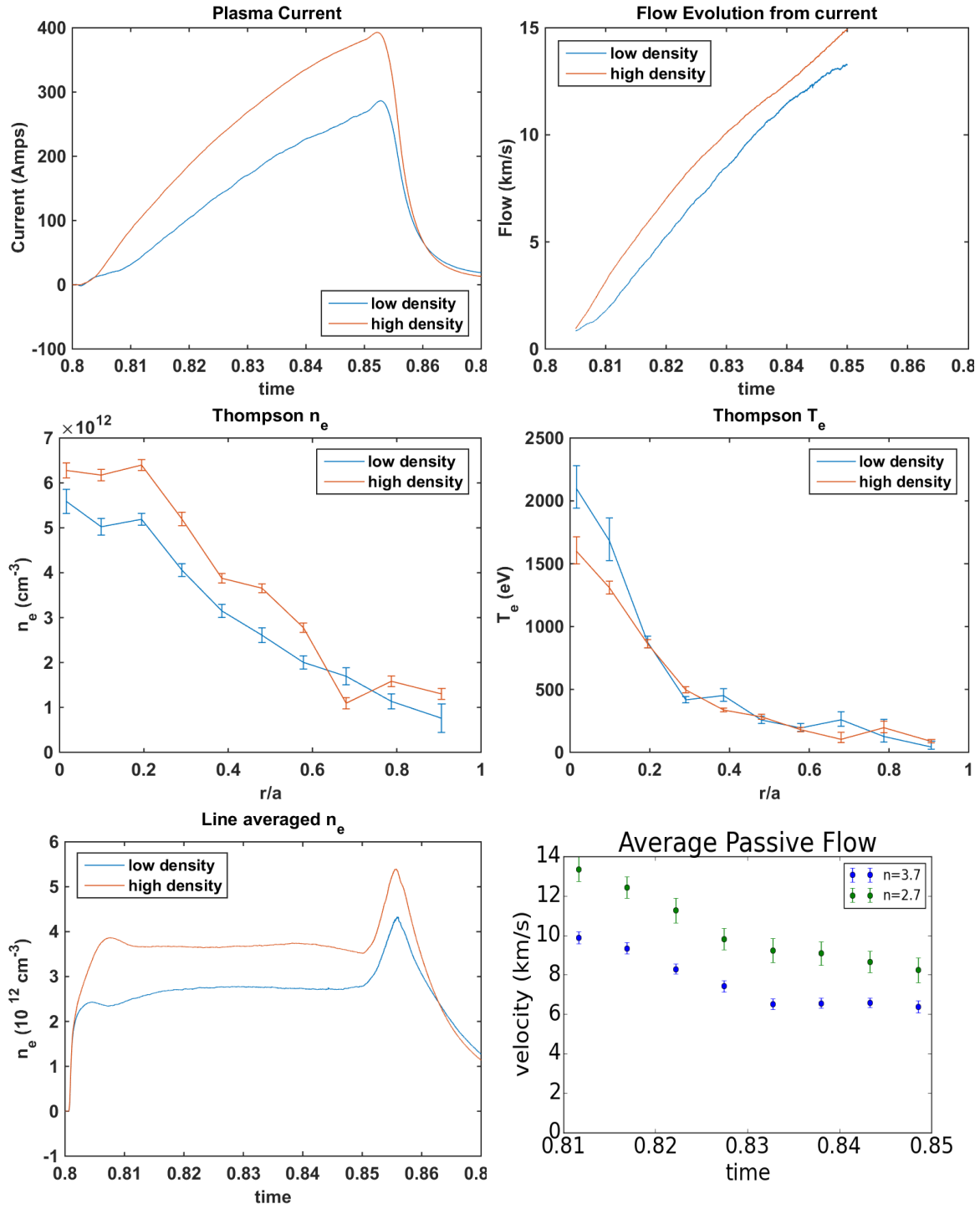


**Figure 4.1** density scan 100 kW QHS, density scan.

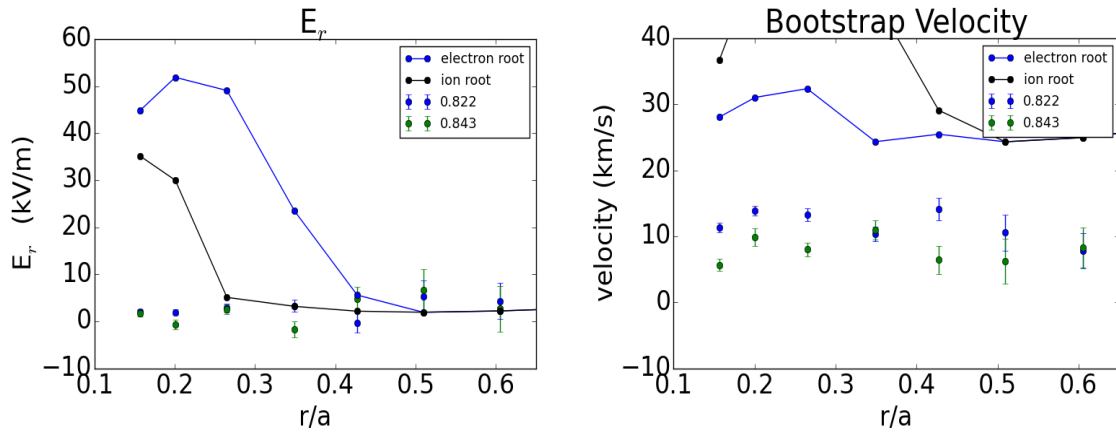


**Figure 4.2** 50 kW QHS active 50 kW QHS active PENTA. NEED 50KW PENTA COMPARISON



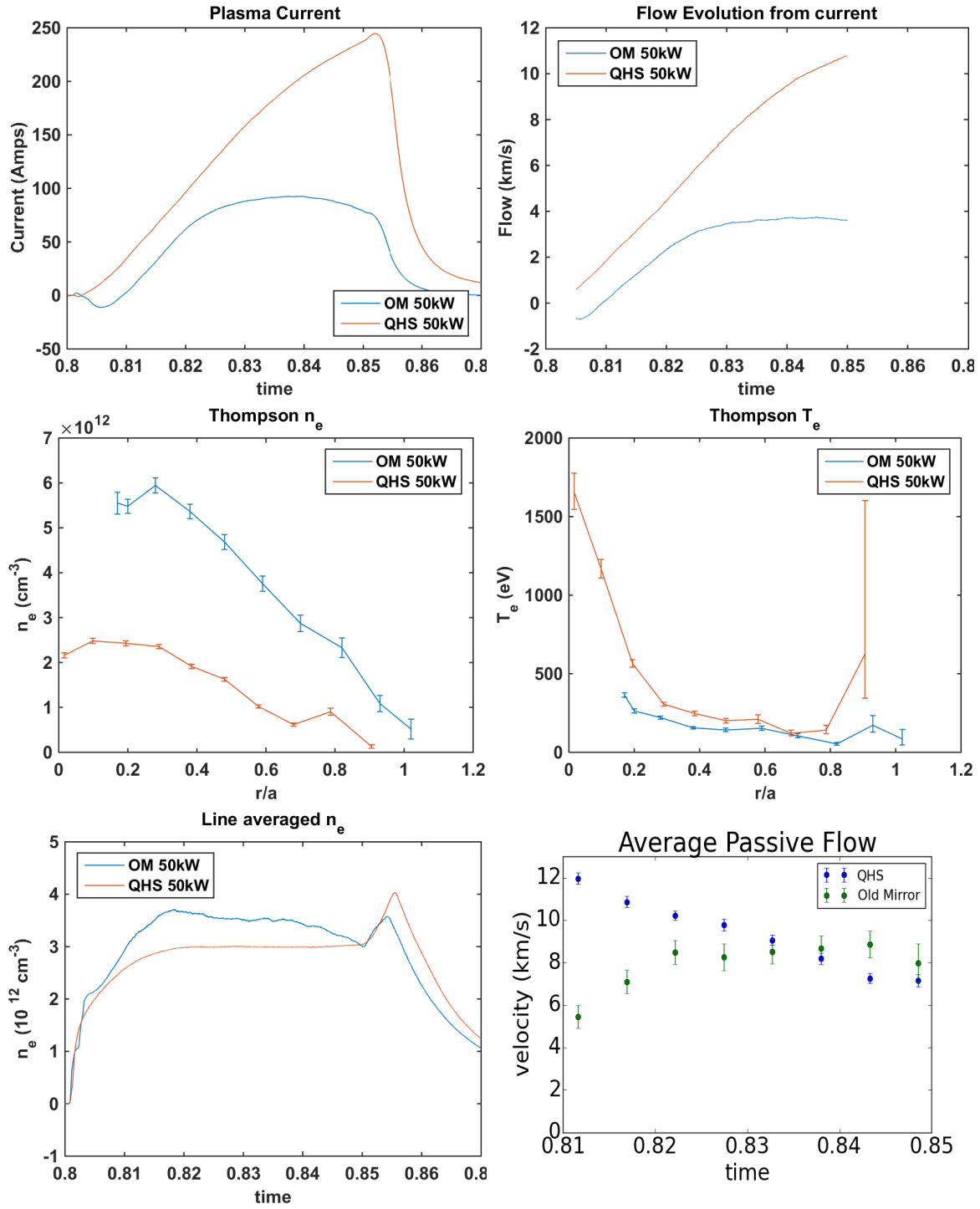


Figure 4.3 50 kW QHS and OM 50 kW QHS and OM.

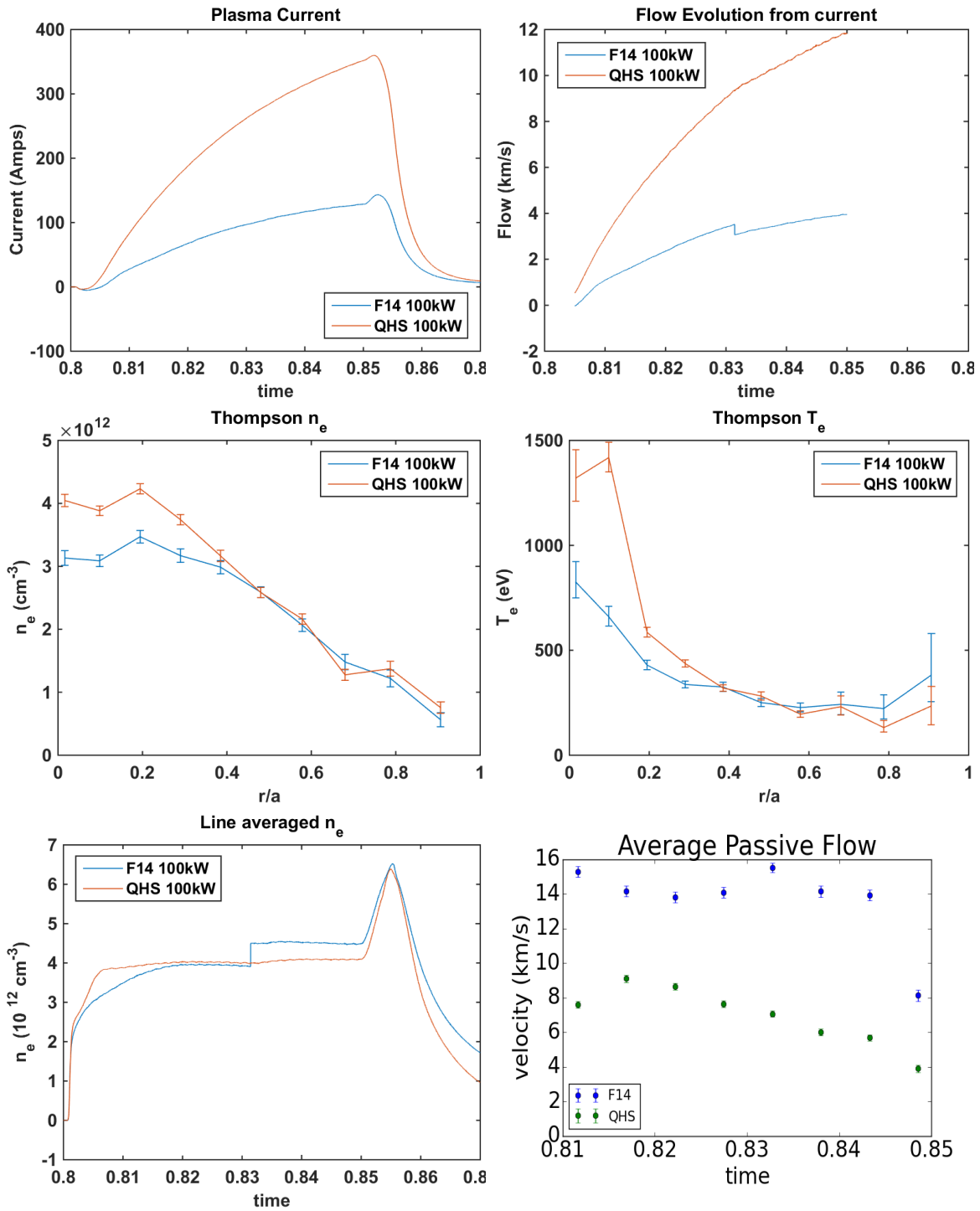
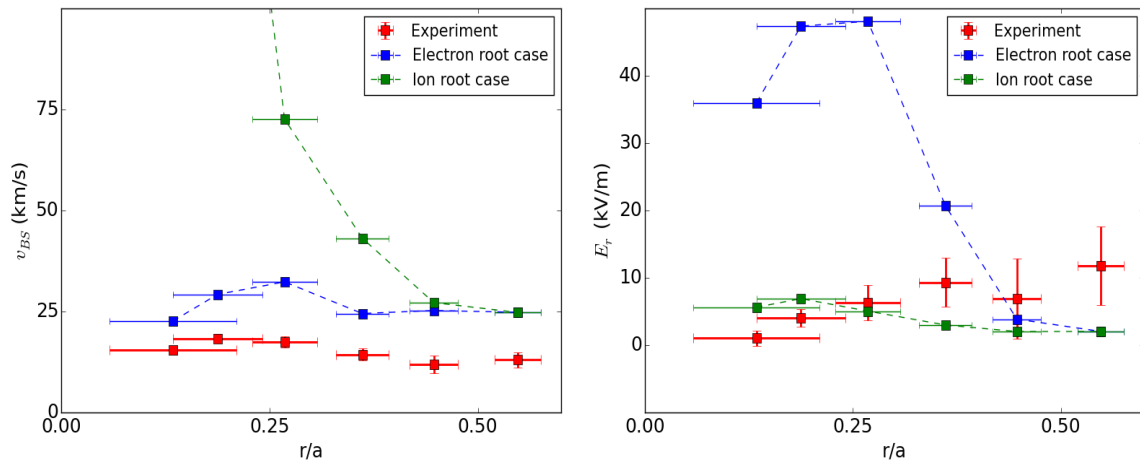
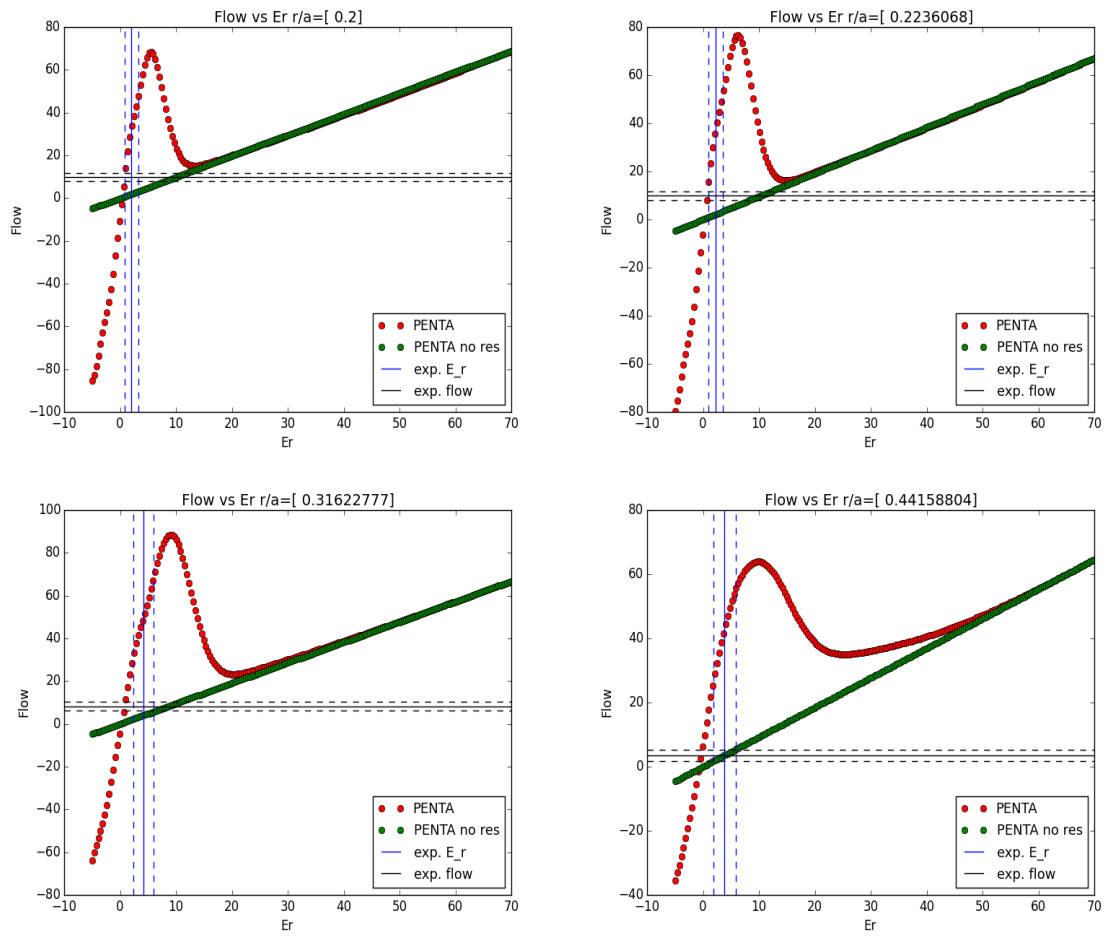


Figure 4.4 100 kW F14 QHS 100 kW F14 QHS.



**Figure 4.5 Pfirsch-Schlüter measurement of flow and  $E_r$ .** The Pfirsch-Schlüter system was used to measure bootstrap flow and  $E_r$ , and the results were compared to the synthetic diagnostic values predicted if the ion or electron root from PENTA calculations were present.



**Figure 4.6** Flow vs  $E_r$  comparisons in QHS. 100 kW QHS.

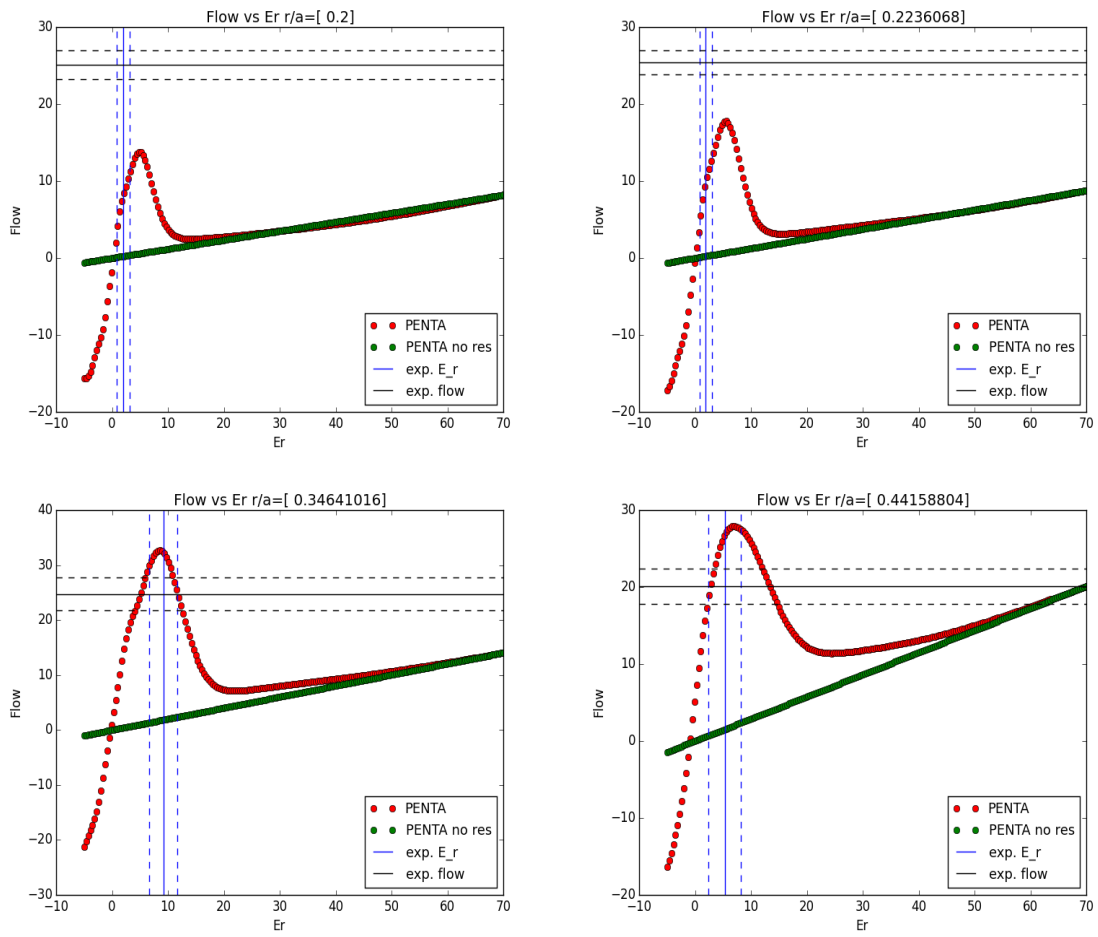


**Figure 4.7** Flow vs  $E_r$  comparisons in F14. 100 kW F14.

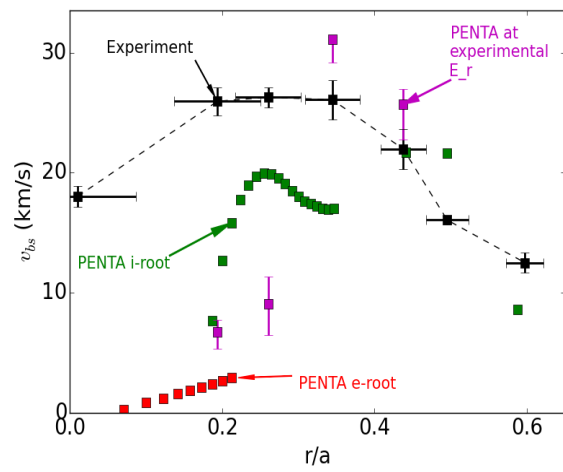


**Figure 4.8 F**

**14 flow predicted by PENTA with experimental  $E_r$ .]** **F14 flow predicted by PENTA with experimental  $E_r$ .** The bootstrap flow is compared to the PENTA predictions of flow 100 kW F14. Figure reproduced from ISHW paper.

## 5.1 Flow Drive

The ionization region effects flow, though this is typically ignored in most devices where the ionization region is in the edge. On HSX, the neutrals are not localized to the edge so this could have an effect on plasma flow. Additionally, the localization of the ionization near the gas injector in the toroidal direction can be seen with the measurements of  $H_{\alpha}$  light on HSX [34]. Experimentally, the plasma current measurements have been made in plasmas with the magnetic field in the reversed direction and when the puffing location was held constant and near the ECRH, the plasma currents could not be matched. When the puffing location was moved to the far side of the device, away from the ECRH mirror, the currents matched between the two cases. This strongly suggests that the ionization region is effecting the current in the plasma and thereby the flow. This effect was on the order of 25% in QHS plasmas (400 A vs 300 A) despite matching Thompson profiles.

The effect on plasma flow needs to be investigated, but a similar asymmetry has been seen in flow, but this asymmetry has other potential explanations [Alexis thesis]??? The flow is about 4 km/s lower throughout the discharge (see figure 5.1).

## **5.2 Conclusion and future work**

The end.



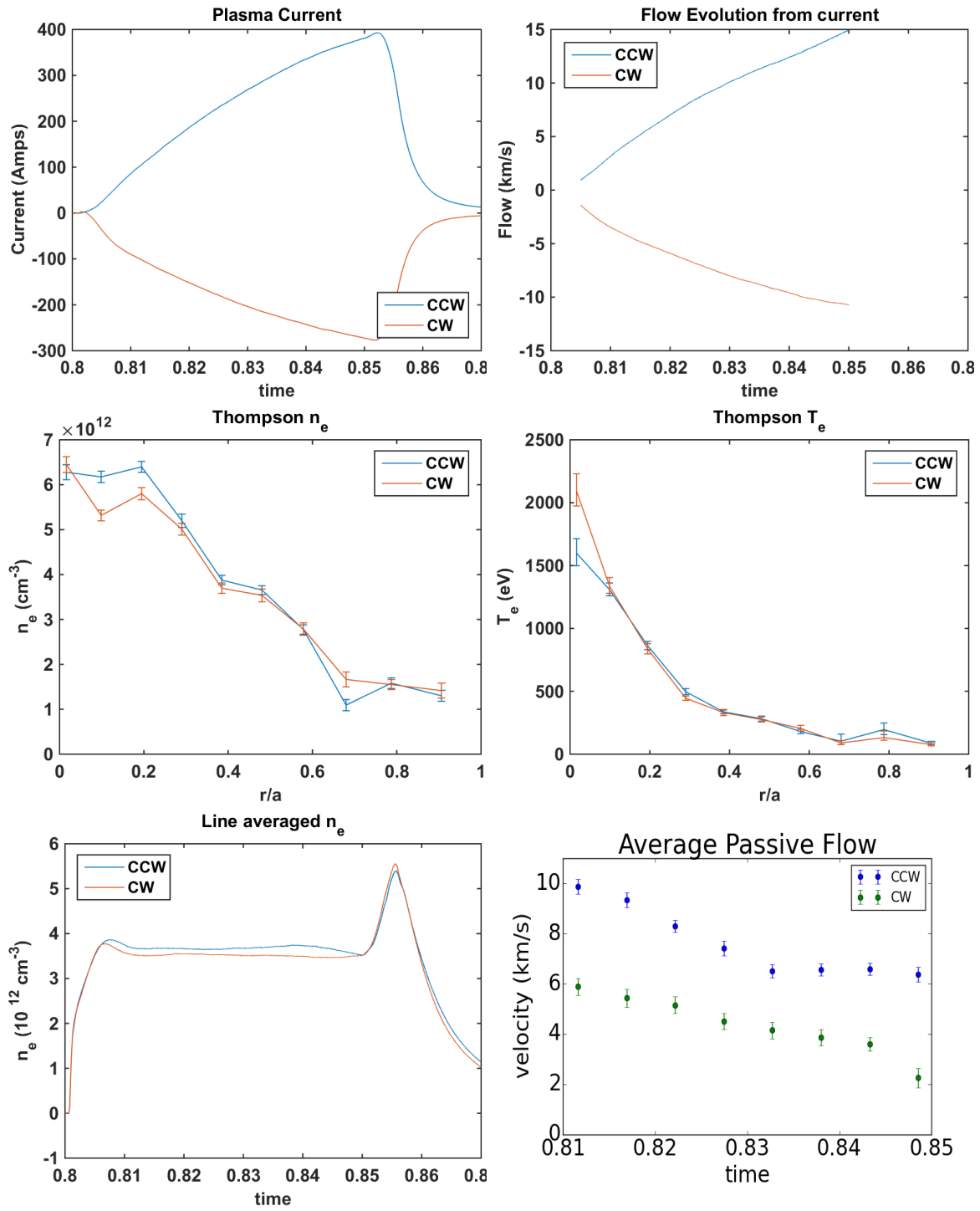


**Figure 5.1** 100 kW QHS CW vs CCW 100 kW QHS CW vs CCW.

## References

34. Gerhardt, S. P. *Measurements and Modeling of the Plasma Response to Electrode Biasing in the HSX Stellarator* PhD thesis (UW-Madison).